



ENSMA, ECLille, ENSIP

**Characterization of wake dynamics for aligned and staggered  
wind turbine arrays via low-dimensional modeling**

Author

**Nicholas M. Hamilton**

A Thesis Submitted in  
Partial fulfillment of the  
Requirements for the Degree of

Master of Science

Supervisor

**Raúl Bayoán Cal**

Co-Supervisor

**Murat Tutkun**

Submitted:  
September 2012



# Abstract

Model wind turbine arrays were developed for the purpose of investigating wake interaction and atmospheric boundary layer recovery dynamics given various configurations of turbines within the array. The work presented here compares the dynamics between a standard rectilinear array and two row-offset configurations. Stereo particle-image-velocimetry was used to collect a large sample of data ahead of and behind entrance and exit row turbines in each configuration. Inflow and wakes were compared statistically and through proper orthogonal decomposition (POD). Spacing within the array configurations lead to varied wake recovery conditions visible in statistics and POD analysis. The number of snapshot POD modes required to reconstruct specified energy levels for the wakes demonstrates a strong dependence on the array configuration. Quantities including flux of kinetic energy and production rebuild with fewer POD modes than vorticity and dissipation as they rely on large-scale structures for shape and intensity. Energy content and organization in small-scale structures contribute to the delay of recovery of the flow to upstream inflow conditions.

# Table of Contents

<b>Introduction</b>	<b>3</b>
<b>1 Theory</b>	<b>5</b>
1.1 Wind Turbines in the ABL . . . . .	9
1.2 Power production of wind turbines . . . . .	11
1.3 The Proper Orthogonal Decompostion . . . . .	13
1.3.1 Classical POD . . . . .	13
1.3.2 The method of snapshots . . . . .	15
<b>2 Design of Experiment</b>	<b>19</b>
2.1 Wind Tunnel Facility . . . . .	19
2.2 Inflow Conditioning . . . . .	20
2.2.1 Inflow characterization . . . . .	21
2.3 Flow measurement system . . . . .	22
2.4 Wind turbine models . . . . .	23
2.5 Torque sensing system . . . . .	24
2.6 Test Cases . . . . .	25
2.7 Data Sets and Convergence . . . . .	26
<b>3 Results of Power Measurements</b>	<b>29</b>
<b>4 Results of SPIV</b>	<b>33</b>
4.1 Flow upstream of turbines . . . . .	34
4.2 Wake comparisons . . . . .	35
4.3 Reynolds stresses comparisons . . . . .	39
4.4 Flux of kinetic energy . . . . .	43

4.5 Additional quantities of interest . . . . .	47
<b>5 Results of Snapshot POD</b>	<b>51</b>
5.1 Validation of POD methods . . . . .	51
5.2 POD results . . . . .	55
<b>6 Conclusion and Discussion of Results</b>	<b>67</b>
6.1 Summary of research . . . . .	67
6.2 Future Works . . . . .	69
<b>Bibliography</b>	<b>i</b>

# List of Figures

1	Images of the Alta wind farm. Currently the largest wind farm in existence, producing approximately 1550 MW. Build in nine stages since the 1970's. Photograph: kcctsTM via Flickr . . . . .	2
2	Until recently Denmark had the largest offshore farm - Horns Rev 2 - in the North Sea 30 kilometers off the west coast producing 209MW from 91 turbines. It was brought on-line in September 2009 (construction beginning in May 2008). . . . .	3
3	Photo showing the wakes of the offshore wind farm Horns Rev. Note that the turbines are placed in a regular grid such that successive turbines are downstream from one another. . . . .	4
2.1	Schematic of experimental setup viewed from the user-side of the wind tunnel. Detail of PIV recording area and model wind turbine in figure 2.4. Inflow parameters $u_*$ , $\Delta U^+$ , and $y_0$ are related through equation 2.2. The schematic above is for reference only, dimensions are not to scale.	20
2.2	Schematic of vertical stakes used to generate mean shear flow. Stakes were designed to simulate the atmospheric boundary layer typical of wind farms. Dimensions in detail subfigure (left) are all in mm. . . . .	21
2.3	Inflow of the ABL to the turbine array in linear (left) and logscale (right) units. A fit line was generated according to equation 2.1 in the log layer (specifically, $y$ varies from 0.108 m to 0.233 m). The effective friction velocity, $u_*$ was calculated to be 0.385 m/s and the effective roughness $10^{-4}$ m. This lead to a velocity deficit of $\Delta U^+ = 14.9$ m/s. . . . .	22

2.4	Side view of wind turbine model showing the relative location of SPIV planes and profile locations. Profiles and contour plots shown in Chapter 4. . . . .	23
2.5	Technical drawing of model wind turbines used in experiments. The rotor blades were designed such that the widest part was pitched to $15^\circ$ from the plane of the hub. The tips of each blade were pitched to $10^\circ$ from the plane of the hub. All dimensions are in millimeters. Note that the mounting plate shown in 2.5(a) spans the full width of the wind tunnel and only a small section is shown. . . . .	24
2.6	Schematic, 2.6(a), and picture, 2.6(b), of the torque sensor used in the experiment. The reflective tape show in the top rotor blade in 2.6(b) was used in the optical measurements of angular velocity. . . . .	25
2.7	In all cases, the downstream spacing is equivalent to six times the rotor diameter (0.72 m). The spanwise spacing is three rotor diameters (0.36 m). SPIV planes in subfigures 2.7(a), 2.7(b), and 2.7(c) correspond to the locations of contours described in Chapter 4 and table 4.1. . . . .	28
3.1	Example strain gauge calibration curve. Curve shown corresponds to the entrance row turbine in the offset arrangement. . . . .	29
3.2	Power curves generated by the entrance and exit row wind turbine models. Power measurements for both offset cases are included. The entrance row of the offset data (+) corresponds to the (3-2-3-2) configuration and the exit row (*) corresponds to the (2-3-2-3) configuration. . . . .	30
3.3	Curves of power coefficient $c_p$ by tip speed ratio $\lambda_{tsr}$ according to equations 1.11 and 1.12, respectively. The exit row turbine performance shows a five-fold improvement from the base arrangement to the offset arrangement. . . . .	31
4.1	Contours of mean velocity in the streamwise direction, $U$ . . . . .	35
4.2	Contours of mean velocity in the wall-normal direction, $V$ . . . . .	36
4.3	Profiles of mean velocity in the streamwise direction, $U$ , according to the streamwise coordinate. Profiles shown correspond to the hub of the rotor $\pm$ the radius of the rotor. . . . .	37

4.4 Profiles of mean velocity in the wall-normal direction, $V$ , according to the streamwise coordinate. Profiles shown correspond to the hub of the rotor $\pm$ the radius of the rotor. . . . .	37
4.5 Profiles of mean velocity in streamwise 4.5(a) and wall-normal 4.5(b) directions according to the wall-normal coordinate. Profiles are taken at half-diameter distances ( $x/D = \pm 0.5 \times n, n \in [1, 2, 3, 4]$ ) upstream and downstream of wind turbine model. . . . .	38
4.6 Contour plots of spanwise velocity component, $W$ . Distinctive wake behavior shown in greater clarity in wakes following more organized inflows (BCF in the top-left and OC2 in the bottom-right). . . . .	39
4.7 Contour plots of $\bar{u^2}$ for all SPIV locations as delineated in figure 2.7 and by table 4.1. . . . .	41
4.8 Contour plots of $\bar{v^2}$ for all SPIV locations as delineated in figure 2.7 and by table 4.1. . . . .	41
4.9 Profiles of streamwise normal Reynolds stress, $\bar{u^2}$ according to the streamwise coordinate. Profiles shown correspond to the hub of the rotor $\pm$ the radius of the rotor. . . . .	42
4.10 Profiles of streamwise normal Reynolds stress, $\bar{v^2}$ according to the streamwise coordinate. Profiles shown correspond to the hub of the rotor $\pm$ the radius of the rotor. . . . .	43
4.11 Profiles of Reynolds normal stresses in streamwise 4.11(a) and wall-normal 4.11(b) directions according to the wall-normal coordinate. Profiles are taken at half-diameter distances ( $x/D = \pm 0.5 \times n, n \in [1, 2, 3, 4]$ ) upstream and downstream of wind turbine model. . . . .	44
4.12 Contour plots of turbulent kinetic energy, $k = \frac{1}{2}(\bar{u^2} + \bar{v^2} + \bar{w'^2})$ . . . . .	45
4.13 Contour plots of $-\bar{uv}$ for all SPIV locations delineated in figure 2.7. . .	45
4.14 Profiles of turbulent kinetic energy (4.14(a)) and the Reynolds stress $-\bar{uv}$ (4.14(b)). Profiles are taken at half-diameter distances ( $x/D = \pm 0.5 \times n, n \in [1, 2, 3, 4]$ ) upstream and downstream of wind turbine model.	46
4.15 Contour plots of flux of kinetic energy, $F_{ij}$ . As in turbulence production, only the streamwise and wall-normal components are shown as $F_{12} = -\bar{uv}U$ as dominant contributor to the whole. . . . .	47

4.16 Comparison of flux of kinetic energy $F_{12}$ for wake areas only. Wakes correspond to BCF, BCB, and OC2 from left to right. . . . .	48
4.17 Contour plots of spanwise component of vorticity, $\Omega_z = \frac{\partial U}{\partial y} - \frac{\partial V}{\partial x}$ for all SPIV locations delineated in figure 2.7. . . . .	48
4.18 Contour plots of turbulence production. Here, the only component of $\mathcal{P}_{ij}$ shown in $\mathcal{P}_{12} = -\bar{uv}\frac{\partial U}{\partial y}$ . The contribution of $\mathcal{P}_{12}$ to the total turbulence production was between 1 and 4 orders of magnitude greater than other components. . . . .	49
5.1 Comparisons of original statistical data and reconstructed mean using only the first mode of POD with instantaneous data for upstream and downstream positions. . . . .	52
5.2 Relative error between the velocity fields compared in figure 5.1. Error is defined as $Err_{rel} =  U - U_{rec,n=1} /U$ . The downstream position (right) is a detail section of the rotor hub area where numerical error is most significant. In the upstream window, error is bound from approximately 0 – 3%. In the downstream area, the error can be <i>very</i> large due to division by near zero elements in the near wake. . . . .	52
5.3 Comparison of $\lambda$ values based on POD method. Note that the instantaneous data starts at mode 2 (the first mode is the mean flow) and that including the $w$ component increases the relative energy content at smaller modes. Solid lines correspond to upstream positions, dashed lines correspond to downstream positions. . . . .	53
5.4 Comparison of the reconstructed Reynolds stress $-\bar{uv}$ according to four different POD schemes. From top left, clockwise, three component POD of fluctuating data, two component POD of fluctuating data, two component POD of instantaneous data, three component POD of instantaneous data. In each case, only modes required to rebuild 50% of the total energy were used. Reconstructed velocities correspond to the near-wake area of the exit row turbine in the base arrangement. . . . .	54

5.5 Comparison of $\lambda$ values for each measurement position. The subplot on the left is the upstream location for each case and the right is downstream. Note that the first mode for all cases is higher downstream than upstream. Here, all eigenvalues were normalized by the maximum sum, the sum of eigenvalues corresponding to the downstream window of BCF. . . . .	56
5.6 Comparison of $\lambda$ values for each measurement position. The subplot on the left is the upstream location for each case and the right is downstream. Note that the first mode for all cases is higher downstream than upstream. Here, all eigenvalues were normalized by themselves. That is $\sum \lambda_n = 1$ . The black dot-dashed line describes the fall-off of $\lambda$ values as $n^{-1.17}$ . . . .	56
5.7 Contour plots for the first 5 modes resulting from the snapshot POD, in subfigure 5.7(a), $\Phi_u^n$ and in subfigure 5.7(b), $\Phi_v^n$ where $n \in \{1, \dots, 5\}$ . From top to bottom are modes 1 through 5, respectively. From left to right	57
5.8 Vectorial POD modes composed of both $\Phi_u$ and $\Phi_v$ . In each subfigure, the modes increase going downward. The ordinate is normalized wall-normal coordinate, $y/D$ , and the abscissa is the normalized streamwise coordinate $x/D$ . Note the increasing structural complexity moving from mode 1 to mode 10. . . . .	58
5.9 Reconstruction of mean Reynolds stresses $\bar{u}^2$ 5.9(a), $-\bar{uv}$ 5.9(b), and $\bar{v}^2$ 5.9(c). Velocity reconstructions are composed of POD modes $\Phi_u^n$ and $\Phi_v^n$ shown in figure 5.7 according to equation 1.40. The number of modes used in the reconstructions by row from top are, 5, 10, 25, 50, 100, and 200. . . . .	59
5.10 Random coefficient, $a_n$ of the POD. Here shown are the random coefficients corresponding to a single POD mode, $\Phi_u$ or $\Phi_v$ , where the abscissa is the indexed number of SPIV measurements. . . . .	60
5.11 Random coefficient, $a_n$ of the POD. Here shown are the random coefficients corresponding to a single SPIV measurements POD according to mode, $\Phi_u$ or $\Phi_v$ . The decay of $a_n$ with mode number demonstrates that the higher modes contribute less to instantaneous velocity field reconstructions than lower modes. Note that certain fields shower higher values of $a_n$ at intermediate modes than others. . . . .	61

5.12 Normalized mean distribution of random coefficients according to equation 5.1. The left figure shows the distributions of upstream and downstream normalized mean random coefficients in semi-log scaling and the right figure in logscale. Note the trends of the normalized mean distributions are similar in form to the distributions of the eigenvalues, $\lambda$ . Figure 5.13 compares the two trends. . . . .	62
5.13 Comparison overlay of the normalized mean random coefficients $a_{n,norm}$ and the eigenvalues $\lambda$ . Although the fall-off of the two are different, they show similar forms both upstream where the fall-off is very consistent and in the downstream position where the intermediate modes have a more significant contribution. . . . .	63
5.14 Reconstructions of the flux of kinetic energy $F_{ij}$ for all measurement positions. Plotted data comprised of $-\bar{uv}$ with only the modes containing the first 50% energy and the mean velocity field $U$ from SPIV results in Chapter 3. . . . .	64
5.15 Reconstructions of the flux of kinetic energy $F_{ij}$ for the immediate wake areas. Plotted data is the same as in figure 5.14 From left to right, the entrance and exit rows of the base arrangement, and the exit row of the second offset arrangement (2-3-2-3). . . . .	65
5.16 Trends comparing each successive value of $\lambda$ upstream and downstream. The ratio $\kappa = \lambda_{upstream}/\lambda_{downstream}$ emphasizes the difference of power output of a turbine is linked to small scale organization. A higher ratio of $\kappa$ at high mode number indicates that <i>more</i> energy is converted from the mean flow and large-scale turbulence to small scales. . . . .	66

# List of Tables

2.1	Relative error convergence of measurements based on size of data set. . . . .	27
2.2	Relative error convergence of fluctuating velocities based on size of data set. . . . .	27
4.1	Presentation of SPIV planes in all contour figures. . . . .	34
5.1	Total energy, $E = \sum \lambda_n$ , in the upstream and downstream positions of BCB according to POD method. . . . .	51
5.2	Modes required to reconstruct a prescribed portion of turbulence energy (upstream–downstream) . . . . .	55
5.3	Ratio of sums of eigenvalues in upstream and downstream measurement locations. . . . .	65

# Introduction

Wind turbines have been a source of energy for centuries and have within the last 50 years been a major contributor of energy free from fossil fuels. When grouped together in large numbers, wind turbines in the form of farms or arrays have become a small but significant portion of the global energy budget. Wind turbines produced a combined total of approximately 240 GW globally as of 2011. Places on the planetary surface subject to consistent wind are often the ideal locations for such wind farms.

The 1970's saw the implementation of large-scale wind farms in many countries around the world. The Alta wind farm in California, USA, is one such wind farm designed with the intent to scale up over successive decades. The Alta wind farm is now the worlds largest producer of wind power, producing some 1.55 GW combined from its nine subsidiary installations. Figure 1 shows several of the subsidiary installations of the Alta wind farm.

Although able to generate up to 3 MW of power each, wind turbines are still being characterized and analyzed as they work together in large arrays. Due to constraints from topography, installation expense, and policy, turbine arrays are often forced to conform to less than ideal shapes and individual turbines can be placed too close together in order to maximize global output power rather than efficiency.

Building wind turbine arrays off the coastline has been a growing trend since 1991. High free-stream velocities and relatively low surface roughness (when compared to on-shore installations) makes offshore locations an arena in which wind can contribute a great deal of power. Their removal from land means that problems such as noise and aesthetic issues are mitigated along with freeing flat land for agriculture and other uses. However, building large-scale arrays offshore also means that the price per Watt of power produced is increased and that access and maintenance are made more difficult.

As of 2010, the global production of wind power from offshore installations topped



Figure 1: Images of the Alta wind farm. Currently the largest wind farm in existence, producing approximately 1550 MW. Built in nine stages since the 1970's. Photograph: kcdsTM via Flickr

3 GW, with the majority coming from European countries or companies. The largest operational offshore farm today is the Walney wind farm, 14 km off the coastline in the Irish Sea. With just over 100 turbines, the Walney wind farm produces over 360 MW. Figures 2 and 3 show several other offshore wind farms in operation. Due mostly to the expense of installing wind turbines offshore, the turbines themselves are arranged in an effort to balance the cost of the installation and the configuration of turbines rather than to maximize their global performance. In some cases, this leads to sub-optimal siting of turbines within the arrays. Figure 3 shows that many of the turbines in the array are directly downstream of leading devices. This leads to a reduced inflow energy and thus decreased global performance of the array.

Wind turbines operate in the atmospheric boundary layer (ABL) and are thus subject to strong gradients of velocity and large fluctuations in the sense of turbulence and sweeping changes of mean velocity in the form of gusts and atmospheric changes by time of day and season. While individual turbines and wind farms grow in scale to maximize gross power output, much remains to be investigated regarding the interactions of turbines or large-scale arrays with turbulence in the ABL or the complex wake dynamics within a turbine canopy.

As the investment in large scale wind farms increases and they become a significant contributor to the total energy production, the need to understand their complex flow dynamics also increases. There are many issues that are yet resolved regarding siting and turbulence in wind power production. The ABL has been the object of atmospheric sciences and meteorology for decades and is now well characterized for input to turbine arrays. Wind turbine wakes complicate the flow available to successive devices, and



Figure 2: Until recently Denmark had the largest offshore farm - Horns Rev 2 - in the North Sea 30 kilometers off the west coast producing 209MW from 91 turbines. It was brought on-line in September 2009 (construction beginning in May 2008).

need further study in order to increase the global efficiencies of large-scale installations.



Figure 3: Photo showing the wakes of the offshore wind farm Horns Rev. Note that the turbines are placed in a regular grid such that successive turbines are downstream from one another.

# Chapter 1

## Theory

Wind turbines and their wakes have been studied to some extent on an individual basis [2, 42, 43]. A review of aerodynamic considerations in turbine design and analysis is presented in [40]. The combined effects of wake-dynamic interaction within the turbine canopy, however, is still a matter of study. Wind turbine arrays have been modeled numerically as in [3, 17, 19, 37]. Many of the current models use self-similar velocity deficit profiles obtained from experimental and theoretical work. The growth rate of wakes in turbine arrays are generally determined as being caused by the ambient turbulence, which is in turn produced by the shear in the wake from the turbine itself. Generally, the magnitude of the maximum velocity deficit in the wakes is obtained from global momentum conservation.

The wind turbine array has been optimized in the sense of spacing of component turbines to maximize efficiency as in [32]. Large wind farms have been shown to increase the effective surface roughness for the ABL and decreasing the wind velocity at turbine-hub height when compared to an unloaded ABL. Often, increasing the turbine-land area density (i.e. decreasing the average wind-turbine spacing) has an opposing effect on the total extracted power per turbine. The optimization undertaken in [32] addresses the problem of wind-turbine spacing in wind farms, where the optimal spacing is a product of economical constraints and the performance of turbines within the array. This study showed that the optimal spacing for turbines may be as large as 15 rotor diameters in the streamwise direction rather than the 6 or 7 diameters typically found in real installations.

In Chamorro and Porté-Agel [12] an experiment was conducted for an individual

wind turbine in order to analyze the wake in the ABL. Mean velocity was assessed using hot-wire anemometry in order to characterize the cross-sectional distribution of mean velocity, turbulence intensity and kinematic shear stress. Different locations downstream of the turbine were tested for two surface roughness cases. The spatial distribution of the velocity deficit and the turbulence intensity, which are important factors affecting turbine power generation and fatigue loads in wind energy parks, were found to exhibit non-axisymmetric behavior. The non-axisymmetric behavior of the distribution of turbulence intensity in the wake was found to be stronger over the rougher surfaces, where the incoming SSow is less uniform at the turbine level.

The near wake of a small horizontal-axis wind turbine over a range of tip speed ratios were assessed in [18]. In the study, the formation and development of the three-dimensional near-wake was measured at six axial locations within two chord lengths of the blades. It was found that at the lowest tip speed ratio, the turbulence level in the wake was very high, suggesting separation from the blades which are operating at high angles of attack. It was also shown that the three-dimensionality did not contribute significantly to the balance of angular momentum in the wake. Ebert and Wood found evidence that by increasing the tip speed ratio, angular momentum that resided in the tip vortices also increased.

Wind turbines extract kinetic energy from the mean flow in the direction perpendicular to the plane containing the rotor. This energy has been correlated to a difference in upstream and downstream kinetic energy fluxes. In large arrays especially, the kinetic energy entrainment is globally downward from the free flow above the wind turbines into the main canopy layer [11,23]. Optimization of the flux of kinetic energy is a pursuit of those who would push the operating efficiency of wind turbines, individually or in large-scale arrays, toward the theoretical maximum. The formulation of the flux of kinetic energy suggests that energy containing structures, especially those associated with the top tip of the rotor area, are responsible for the entrainment of energy downward into the main turbine canopy area.

Turbulent flows can be well-characterized by a continuum of organized structures and motions following both coherent formulations or ensemble mean patterns. The analysis of such structures is typically followed in the statistical sense of determining energy and stresses present either as an ensemble mean or as they interact through the spectrum of turbulence from energetic structures to dissipation into heat. The

increased understanding of interactions of coherent structures leads to understanding and the control or influence of turbulence. The particular effects of turbulence on the power production capabilities of wind turbines leads ultimately to a realization of the theoretical efficiency of turbines and wind farms.

The proper orthogonal decomposition (POD) has proven to be an effective means of identifying coherent structures in turbulent flows and the energy associated with such structures within the energy cascade of turbulence [1, 5, 8, 28]. Further, because POD organizes the structures within turbulence according to energy content, low-dimensional models can be used to reconstruct flow statistics omitting the energy associated with high frequencies or small structures [15].

Performing POD analysis to a set of random data measurements results in a set of ordered modes that correspond to the energy containing events in a flow field. POD can be applied to any multi-point measurements including rakes of hot-wire probes, usually done in the *classical* POD, or scalar visualization data, particle image velocimetry (PIV), or data resulting from numerical simulations, all of which are typically done in the form of *snapshot* POD. The POD has been applied to many flow configurations. Berkooz et al. [5] provide a comprehensive survey of the early applications.

The POD is limited in its ability to organize structures, events, or patterns by the nature of input data as inherently stochastic as noted in [6]. A greater range of scales associated with any particular flow, such as high Reynolds number flows, will typically yield a greater number of energy containing POD modes, whereas low Reynolds number data will exhibit a greater concentration of energy in fewer modes. The analysis may also neglect infrequent events, regardless of their dynamical importance [28]. Additionally, the POD applied to random data showing homogeneous behavior in any particular dimension or direction reduces to a Fourier decomposition. In such a case, Fourier transforms are typically applied in such a direction for numerical efficiency, but often lead to a poor description of local flow structures and must retain a large number of modes to describe the dynamics [13].

Liu et al. [29] applied the POD method to a turbulent channel flow experiment at high Reynolds numbers. Data with high spatial resolution was collected via two-dimensional PIV to measure a turbulent velocity in streamwise and wall-normal components. The study focused on the similarity of the eigenspectra and eigenfunctions and demonstrated that the proper scaling of the eigenspectra resulted in a collapse in

the eigenspectra.

Axisymmetric far-wakes have been investigated with the POD in [41], in which many separate applications of the POD were applied to experimental hot-wire data to determine the dependence of rate of energy accumulation by POD modes on components of velocity. The accumulation of energy was tested for individual components of velocity in a scalar sense, two- and three-component vectorial POD schemes were also tested and compared to the sum of modal energy content of scalar POD applications. In most applications of the POD to turbulent flow data, the inclusion or exclusion of any particular component of velocity data doesn't greatly affect the distribution of energy content in the range of modes. In the study of the axisymmetric far-wake however, it was found that the azimuthal modal distribution was a function of velocity component inclusion.

In the study by [34] the recirculation zone of an annular jet was measured via PIV and analyzed using the POD. It was determined in the study that there was a distinct relationship between the resultant eigenmodes and the radial fluctuations of the jet. The POD analysis showed that the flow could be decomposed into four main modes in which 90% of the total energy was represented. Further, it was demonstrated that each mode was responsible for a characteristic motion of the recirculation zone.

The POD has been applied to field measurements of wind turbine inflows by [38] in a grid of point-measurements spanning the rotor area. The results were used to formulate a low-dimensional representation of the inflow and subsequently fed into fatigue and loading simulations for the rotor blades. The result of this application of the classical POD yielded many results of the effects of turbulence on the loading and life cycles of a turbine. Because the outflow of the turbine was not investigated in this study, no correlations were made between the energetic POD modes and the power output of the turbine. The spanwise and vertical components of inflow velocity were omitted from the POD on the assumption that they were already in their principle components. Reconstructions of up to the first five modes were used in the bending fatigue load simulations.

Identifying the turbulent wake structures influencing the performance of turbines in an array is followed in the present research. It is currently understood that the large structures are responsible for a majority contribution to wake recovery by the entrainment of kinetic energy from above. An experiment was designed at Portland

State University (PSU) to test the performance of wind turbine models in various configurations within an array. Coupled with measurements of power output are flow measurements in the form of stereographic particle image velocimetry (SPIV). Energy containing structures are distinguished and analyzed using snapshot proper orthogonal decomposition (POD) and reconstructions of the flow and quantities including the flux of kinetic energy are made using a low-dimensional model.

## 1.1 Wind Turbines in the ABL

The Reynolds-averaged Navier-Stokes boundary layer equation in the streamwise direction can be written as shown in equation 1.1. Note that the terms involving viscous dissipation and diffusion are omitted here as all measurements are made sufficiently far from solid boundaries to neglect viscous contributions to the global energy balance.

$$U_j \frac{\partial U_i}{\partial x_j} = -\frac{1}{\rho} \frac{\partial P}{\partial x_i} - \frac{\partial \bar{u}_i \bar{u}_j}{\partial x_j} - \bar{f}_x \quad (1.1)$$

Above,  $\bar{f}_x$  is representative of the thrust force added to the flow in the streamwise direction by the presence of the wind turbines. Typically this force is in the streamwise direction only, thus in the equation above, the subscript corresponds only to  $x$  [11, 44].

In this formulation of the boundary layer equation and all subsequent equations, the engineering convention is used so that  $u$ ,  $v$ , and  $w$  correspond to the streamwise ( $x$ ), wall-normal ( $y$ ), and spanwise ( $z$ ) velocity components, respectively, rather than the atmospheric sciences convention where  $z$  is typically the vertical direction.

In the following equations, a capital letter indicates an ensemble mean value and a lower case letter indicates a turbulent fluctuation from the mean values according to the classical Reynolds decomposition. In this decomposition, the instantaneous value of any unknown quantity (velocity or pressure, denoted here with a tilde) is composed of an ensemble mean value in time and a zero-centered fluctuation,

$$\tilde{a}(x, y, z, t) = A(x, y, z) + a(x, y, z, t) \quad (1.2)$$

An overline implies that an ensemble mean has been taken of the product of two or more fluctuating components.

Multiplying equation 1.1 by the mean streamwise velocity  $U_i$  and rearranging yields

the mean mechanical energy equation in which the mean kinetic energy in the flow is described by the sum of  $\frac{1}{2}U_i^2$ .

$$U_j \frac{\partial \frac{1}{2}U_i^2}{\partial x_j} = -\frac{1}{\rho} U_i \frac{\partial P}{\partial x_i} + \bar{u}_i \bar{u}_j \frac{\partial U_i}{\partial x_j} - \frac{\partial U_i \bar{u}_i \bar{u}_j}{\partial x_j} - \mathcal{F}_{x_i} \quad (1.3)$$

The left hand side of equation 1.3 is composed of the convection of the mean kinetic energy in the flow. On the right side of the equation there are three terms remaining, the diffusion of energy by the mean pressure, the production of mean kinetic energy, and the derivative of the kinetic energy flux. While this equation holds true theoretically for the mean kinetic energy in a turbulent boundary layer, further simplifications can be made based on a closer look at the wakes analyzed in the below sections. The last two terms of equation 1.3 are explored to some extent in §4.5. The mechanical energy removed from the flow,  $\mathcal{F}_{x_i}$ , is generally assessed through direct power measurements of the turbines themselves.

Of interest in the following study are terms and quantities used to characterize the turbulence in wakes and of wind turbine models including mean velocities, Reynolds stresses, and turbulent kinetic energy,  $k$ , defined as half the trace of the Reynolds stress tensor,  $\tau_{ij}$ ,

$$k = \frac{1}{2} \text{tr}(\tau_{ij}) = \frac{1}{2} (\bar{u}^2 + \bar{v}^2 + \bar{w}^2) \quad (1.4)$$

As wind turbines are designed to extract energy from the mean flow, a high level of turbulence suggests that there may be energy locked into flow structures that is not directly or immediately available to wind turbines. Thus comparing  $k$  to the mean kinetic energy can provide some idea of how available the energy in the flow is to the wind turbine array. This idea is explored more with the snapshot POD in §1.3.2 and Chapter 5.

To aid the visual understanding of the mean turbulence in the wakes following the turbines, quantities such as vorticity are of great use. Many studies of fluid mechanics, both numerical and experimental, use contour plots or three dimensional isocontours (when possible) of vorticity to identify structural qualities in turbulence. The mean vorticity in a flow is defined as the curl of the mean velocity,

$$\Omega_i = \frac{\partial U_k}{\partial x_j} - \frac{\partial U_j}{\partial x_k} \quad (1.5)$$

The spanwise component of vorticity  $\Omega_z$  acts in the  $x - y$  plane and can be used to understand the relationships of other quantities such as the mean wall-normal velocity,  $V$  and the flux of kinetic energy,  $F_{ij}$ .

To verify the energy balance suggested by equation 1.3, quantities such as the kinetic energy flux and turbulence production need to be examined. The flux of kinetic energy is generally denoted as,

$$F_{ij} = -\overline{u_i u_j} U_i \quad (1.6)$$

$F_{ij}$  is also an indicator of the degree to which kinetic energy from outside the wake is entrained into the flow. As energy is transported from above the turbine canopy into the wake layer, the wakes themselves are dissipated and the boundary layer recovers to its upstream state.

The turbulence production tensor is generally written as,

$$\mathcal{P}_{ij} = -\overline{u_i u_j} \frac{\partial U_i}{\partial x_j} \quad (1.7)$$

and quantifies the rate at which the mean flow kinetic energy has been converted into turbulence. The production is of interest in the following study as, when viewed from the perspective of the turbine itself, the production characterizes well the dissipation of energy available for power production.

## 1.2 Power production of wind turbines

The power produced by wind turbines operating in the ABL is a function of both the aerodynamic design of the rotor blades and the inflow to the turbine. The power output of the wind turbines can be measured in either of two senses (see [26] for more detail), as electrical power,

$$P_{elec} = \frac{V_{out}^2}{R} \quad (1.8)$$

in which  $V_{out}$  is the output voltage of the generator forming the nacelle of the wind turbine and  $R$  is the effective resistance of the circuit containing the generator, or as mechanical power,

$$P_{mech} = T_{wt} \omega \quad (1.9)$$

in which  $T_{wt}$  is the mechanical torque of the turbine rotor and  $\omega$  is the angular momentum of the rotor.

As generators are mechanical devices subject to losses of energy, several factors act to significantly decrease the generator efficiency [26, 10]. These factors include losses in the copper coils via the dissipation of heat in the windings of the generator, magnetic losses in the induction processes converting magnetic fields to electrical current, and mechanical losses from friction between the bearings suspending rotating parts and the bushings or brushes of the generators. Also included in friction-type losses is the air-friction loss of the rotating armature forming the wind turbine rotor. Due to losses of these types, the measured values of  $P_{elec}$  are expected to be significantly lower than directly measured values of  $P_{mech}$ .

The net power *available* to the wind turbine is commonly defined as,

$$P_{fluid} = \frac{1}{2} \rho \bar{u}_1^3 A \quad (1.10)$$

where  $\rho$  is the density of the air, considered here to be constant,  $\bar{u}_1$  is the free-stream velocity upstream of the turbine and  $A$  is the rotor disc area,  $A = \frac{\pi}{4} D^2$ .  $P_{fluid}$  is derived directly from the conservation of momentum along streamlines in Bernoulli's principle.

The power coefficient of a wind turbine can be computed directly with the above equations as,

$$c_p = \frac{P_{wt}}{P_{fluid}} = \frac{T_{wt}\omega}{\frac{1}{2} \rho \bar{u}_1^3 A} \quad (1.11)$$

where  $\bar{u}_1$  is the mean streamwise velocity over the turbine rotor area. Typically the mechanical power,  $P_{mech}$ , of the turbine is used as the wind turbine power,  $P_{wt}$ , as it is expected to scale much better between wind tunnel experiments and real turbine installations being free from the difficult to diagnose losses detailed above. Thus with measurements of mechanical torque  $T_{wt}$  and angular velocity,  $\omega$ , the power coefficient can be calculated when coupled with flow velocity measurements.

The tip speed ratio of wind turbines is a characteristic number with which experiments are commonly scaled and performance of turbines are gauged [2]. The tip speed ratio is commonly defined as,

$$\lambda_{tsr} = \frac{\frac{D}{2} \omega}{\bar{u}_1} \quad (1.12)$$

and is the ratio of tangential velocity of the tips of the rotor blades to the mean stream-

wise velocity across the rotor area. Typical values of tip speed ratios range from  $4 < \lambda_{tsr} < 5.5$  with optimal ranges of up to  $\lambda_{tsr} = 7$  [36] depending on rotor blade design and particular flow character.

## 1.3 The Proper Orthogonal Decomposition

The formulation of an orthonormal vector basis from random data was used in many applications such as Principle Component Analysis (as early as 1901) and Singular Value Decomposition before the theory was applied to flow measurements. The proper orthogonal decomposition was introduced to the realm of fluid mechanics as a means of analysis by John L. Lumley in 1967. The presence of large coherent structures in turbulent flows precipitated the formal definition of the eigenvalue problem presented below.

### 1.3.1 Classical POD

The POD operates by constructing a series of functions forming a basis with which the span of random data can be built. In the following section, the  $L^2$  inner product and norm will be denoted respectively as,

$$(\mathbf{f}, \mathbf{g}) = \int_{\mathcal{D}} \mathbf{f}(x)\mathbf{g}^*(x)dx \quad (1.13)$$

$$\|\mathbf{f}\| = (\mathbf{f}, \mathbf{f})^{\frac{1}{2}} \quad (1.14)$$

in which  $\mathbf{f}$  and  $\mathbf{g}$  are vector functions and are defined over the domain  $x \in \mathcal{D}$ . The star signifies complex conjugation.

As it applies to fluid mechanics, the random vector fields are comprised of instantaneous velocities, which are functions of both space and time. Because the focus of the following investigation is the turbulent energy associated with coherent structures, the zero-centered fluctuations proposed in equation 1.2 are considered. The use of *instantaneous* measurements is explored in Chapter 5.

The candidate function to form the vector basis of the POD is denoted as  $\Phi$ . With the fluctuating velocity and vector basis, the quantity to optimize by this decomposition is,

$$\frac{\langle |(\mathbf{u}, \Phi)| \rangle}{\|\Phi\|^2} = \lambda \quad (1.15)$$

where the angle brackets denote ensemble averaging. Following Lumley's presentation of the POD, the kernel theorem allows equation 1.15 to be expressed as,

$$\frac{(\mathbf{R}(\mathbf{x}, \mathbf{x}'), \Phi(\mathbf{x})\Phi^*(\mathbf{x}'))}{(\Phi(\mathbf{x})\Phi^*(\mathbf{x}))} = \lambda \quad (1.16)$$

where  $\mathbf{R}(\mathbf{x}, \mathbf{x}')$  is the two-point correlation tensor,

$$\mathbf{R}(\mathbf{x}, \mathbf{x}') = \langle \mathbf{u}(\mathbf{x})\mathbf{u}^T(\mathbf{x}') \rangle \quad (1.17)$$

In order to apply the calculus of variations, one must verify that  $\Phi(x)$  does indeed maximize equation 1.15. This is accomplished by the introduction of a perturbation of the same form as  $\Phi(x)$ . The derivation following [35] results in an integral equation of the same form as equation 1.13.

$$\int_{\Omega} \mathbf{R}(\mathbf{x}, \mathbf{x}')\Phi(\mathbf{x}')d\mathbf{x}' = \lambda\Phi(\mathbf{x}) \quad (1.18)$$

where  $\Omega$  denotes the spatial domain in consideration as  $\mathbf{x} \in \Omega$ .

Because the two-point correlation tensor,  $\mathbf{R}(\mathbf{x}, \mathbf{x}')$ , is symmetric and bounded to the domain,  $\Omega$ , a number of useful properties arise concerning equation 1.18. These properties are, due to the Hilbert-Schmidt theory and known commonly as the proper orthogonal decomposition theorem and can be summarized in three points:

- A denumerable set of solutions exist such that,

$$\int_{\Omega} \mathbf{R}(\mathbf{x}, \mathbf{x}')\Phi(\mathbf{x}')d\mathbf{x}' = \lambda^i\Phi^i(\mathbf{x}), \quad i = 1, 2, \dots, N \quad (1.19)$$

The solutions can be mutually orthonormal such that the contraction of their norms leads to,

$$(\Phi^j, \Phi^k) = \delta_{jk} \quad (1.20)$$

- The complete set formed by  $\Phi^i$  may be used as a basis for expanding the velocity

field by,

$$\mathbf{u}(\mathbf{x}, t) = \sum_{i=1}^{\infty} a^i(t) \Phi^i(\mathbf{x}) \quad (1.21)$$

where the coefficients  $a^i(t)$  are determined by

$$a^i(t) = (\mathbf{u}(\mathbf{x}, t), \Phi^i(\mathbf{x})) , \quad i = 1, 2, \dots, N \quad (1.22)$$

and satisfy:

$$\langle a^i(t) a^{j\star}(t) \rangle = \delta_{ij} \lambda^i \quad (1.23)$$

- Finally, the eigenvalues,  $\lambda^i$  are nonnegative and their sum is finite.

$$\lambda^i \geq 0, \quad i = 1, 2, \dots, N \quad (1.24)$$

$$\sum_{i=1}^{\infty} \lambda^i < \infty \quad (1.25)$$

One of the most important features of the POD is that the total energy of the two-point correlation, that is the turbulent kinetic energy, is contained in the ordered sum of the eigenvalues as,

$$\int_{\Omega} \mathbf{R}(\mathbf{x}, \mathbf{x}') = \int_{\Omega} \langle \mathbf{u}(\mathbf{x}) \mathbf{u}^T(\mathbf{x}') \rangle = \sum_{i=1}^{\infty} \lambda^i \quad (1.26)$$

It is upon this point that much of the analysis presented in Chapter 5 is based including the low-dimensional models and reconstructions of quantities in §1.1.

### 1.3.2 The method of snapshots

According to [35] and [39] the method of snapshots, referred to from here as *snapshot* POD, is built on a basis of uncorrelated flow measurements in a field. Snapshot POD was introduced by Sirovich in 1987 and applied to scalar visual data with the intent to distinguish energetic structures on which flow fields are build. The stochastic flow field can be written as,

$$\mathbf{u}^n = \mathbf{u}(\mathbf{x}, t^n) = \mathbf{u}(\mathbf{x}, n\tau), \quad n \in [1, \dots, N] \quad (1.27)$$

where  $\tau$  is the typical time separation between measurements, usually at least twice the integral time scale to ensure that measurements remain uncorrelated. Here, the velocity data is a collection of stochastic turbulent fluctuations. With a large number of samples, the two-point spatial correlation tensor can be approximated as,

$$\mathbf{R}(\mathbf{x}, \mathbf{x}') = \frac{1}{N} \sum_{n=1}^N \mathbf{u}(\mathbf{x}, t^n) \mathbf{u}^T(\mathbf{x}', t^n) \quad (1.28)$$

The two-point spatial correlation tensor becomes the kernel of the POD eigenvalue problem solved numerically. It is then assumed that a basis of  $N$  modes can be written in terms of the original data as,

$$\Phi(\mathbf{x}) = \sum_{i=1}^N A(t^i) \mathbf{u}(x, t^n) \quad (1.29)$$

where  $\Phi(\mathbf{x})$  is a deterministic field set sought by the POD. The maximization of the projection of  $\mathbf{u}$  onto  $\Phi$  can be performed by finding the largest inner product of the fields in a mean square sense,

$$\langle |\alpha|^2 \rangle = \langle |u_i, \phi_i^\star| \rangle \quad (1.30)$$

The POD modes  $\Phi(\mathbf{x})$  can then be expressed as solutions to the eigenvalue problem

$$\mathbf{R}(\mathbf{x}, \mathbf{x}') \Phi(\mathbf{x}') = \lambda \Phi(\mathbf{x}) \quad (1.31)$$

An integral equation for the determination of  $\Phi(\mathbf{x})$  can be expressed as,

$$\int_{\Omega} \mathbf{R}(\mathbf{x}, \mathbf{x}') \Phi(\mathbf{x}') d\mathbf{x}' = \lambda \Phi(\mathbf{x}) \quad (1.32)$$

Here  $\Omega$  denotes the domain being considered such that  $\mathbf{x} = (x, y, z) \in \Omega$ . Substituting in definitions for  $\Phi(\mathbf{x})$  and  $\mathbf{R}(\mathbf{x}, \mathbf{x}')$  yields,

$$\int_{\Omega} \frac{1}{N} \sum_{n=1}^N \mathbf{u}(\mathbf{x}, t^n) \mathbf{u}^T(\mathbf{x}', t^n) \sum_{i=1}^N A(t^i) \mathbf{u}(\mathbf{x}', t^i) d\mathbf{x}' = \lambda \sum_{i=1}^N A(t^i) \mathbf{u}(\mathbf{x}, t^i) \quad (1.33)$$

Because the above integration is with respect to  $\mathbf{x}'$  only, equation 1.33 can be rewritten

as,

$$\sum_{n=1}^N \left( \sum_{n=1}^N \left( \frac{1}{N} \int_{\Omega} \mathbf{u}^T(\mathbf{x}', t^n) \mathbf{u}(\mathbf{x}', t^n) d\mathbf{x}' \right) A(t^i) \mathbf{u}(\mathbf{x}, t^n) \right) = \lambda \sum_{i=1}^N A(t^i) \mathbf{u}(\mathbf{x}, t^i) \quad (1.34)$$

which can be further simplified as,

$$\sum_{n=1}^N \left( \frac{1}{N} \int_{\Omega} \mathbf{u}^T(\mathbf{x}', t^n) \mathbf{u}(\mathbf{x}', t^n) d\mathbf{x}' \right) A(t^i) = \lambda A(t^i) \quad (1.35)$$

Introducing the coefficient vector  $\mathbf{A}$ , and the imperial correlation matrix  $\mathbf{C}$ ,

$$\mathbf{A} = [A(t^1), A(t^2), \dots, A(t^n)]^T \quad (1.36)$$

$$\mathbf{C} = \sum_{n=1}^N \left( \frac{1}{N} \int_{\Omega} \mathbf{u}^T(\mathbf{x}', t^n) \mathbf{u}(\mathbf{x}', t^n) d\mathbf{x}' \right) \quad (1.37)$$

The resulting eigenvalue problem can be written simply as,

$$\mathbf{CA} = \lambda \mathbf{A} \quad (1.38)$$

Solving the problem proposed by equation 1.38 yields a complete set of eigenfunctions and corresponding eigenvalues. The eigenfunctions can be used to then create a set of POD modes according to equation 1.29. The POD modes are typically normalized to obtain an orthonormal basis, the final expression of the POD basis.

$$\Phi^i(\mathbf{x}) = \frac{\sum_{i=1}^N A^i(t^n) \mathbf{u}(\mathbf{x}, t^n)}{\| \sum_{i=1}^N A^i(t^n) \mathbf{u}(\mathbf{x}, t^n) \|} \quad (1.39)$$

The stochastic velocity fields can be reconstructed using the eigenfunctions of the POD,

$$\mathbf{u}(\mathbf{x}, t^n) = \sum_{n=1}^N a_n \Phi^n(\mathbf{x}) \quad (1.40)$$

where  $a_n$  are a set of random coefficients obtained by back-projecting the set of deterministic POD modes onto the stochastic velocity fields,

$$a_n = \int_{\Omega} \mathbf{u}(\mathbf{x}, t^n) \Phi^n(\mathbf{x}) \quad (1.41)$$

The random coefficients delineated by equation 1.41 are uncorrelated due to the orthogonality of the eigenfunctions. Thus we can write,

$$\lambda^n = \langle a_n, a_m^* \rangle \delta_{nm} \quad (1.42)$$

The cross correlation tensor,  $R_{ij}$  can also be reconstructed using the eigenfunctions and eigenvalues obtained through the POD.

$$\mathbf{R}_{ij}(\mathbf{x}, \mathbf{x}') = \lambda^n \Phi_i^n(\mathbf{x}) \Phi_j^n(\mathbf{x}') \quad (1.43)$$

Contraction of the reconstructed correlation tensor,  $R_{in}$  shows that the total energy in the domain,  $\Omega$  is equal to the summation of the eigenvalues,  $\lambda^n$ , as

$$E = \int_{\Omega} \langle \mathbf{u}_i(\mathbf{x}) \mathbf{u}_i(\mathbf{x}) \rangle = \sum_{n=1}^N \lambda^n \quad (1.44)$$

Thus, the POD provides an optimal set of eigenfunctions that decompose the energy in the turbulence domain and the eigenvalue measures the energy associated with each mode.

## Chapter 2

# Design of Experiment

### 2.1 Wind Tunnel Facility

The facility at Portland State University (PSU) has been built to research emerging problems of turbulent fluid flows in both fundamental and applied cases. The facility consists of a return type wind tunnel with a contraction ratio of 9:1 to ensure low turbulence intensities. The test section has a length of 5 m and a cross section of 0.8 m  $\times$  1.2 m. The test section speed may be adjusted in a reliable working range of 2 m/s to 40 m/s. The test section is comprised of a variable-profile articulated ceiling, fixed non-operators'-side wall, floor, and operators'-side wall consisting of access panels. This ensures easy access to the tunnel and the capability of imposing positive and/or negative stream-wise pressure gradients. The test chamber cross-sectional area gradient is adjustable in the range of  $0.55 \text{ m} > dA/dx > -0.55 \text{ m}$  with the distance between the test section floor and ceiling able to be modified between 0 and 0.8 m. A rigid, steel framework is designed to serve as the supporting framework for the test section components, and a precision platform for the setup and operation of experiments. All surfaces are constructed of schlieren grade annealed float glass affixed to the steel framework to ensure maximum access to the non-intrusive laser measurement techniques.

Figure 2.1 shows the experimental setup from the user's side of the wind tunnel. Features shown in the schematic from left are the passive grid at the end of the contraction at the beginning of the test area, vertical strakes for shaping the inflow (discussed further in §2.2), chains to simulate surface roughness, and the wind turbine models (detailed in figure 2.5). Also shown are several of the locations velocity measurements were made

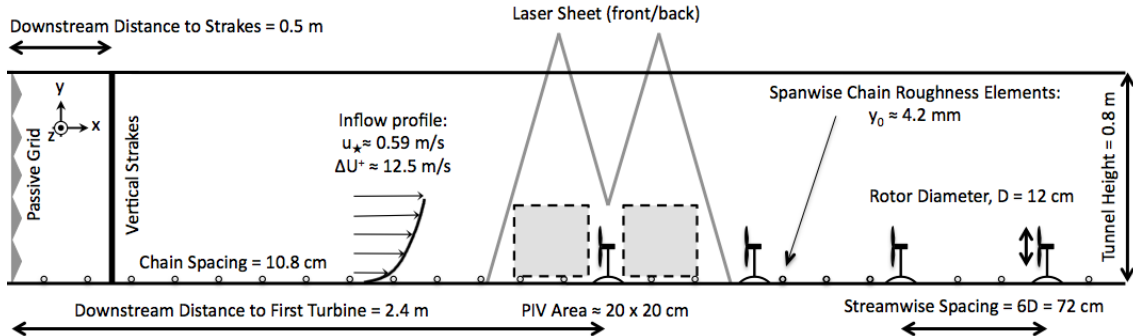


Figure 2.1: Schematic of experimental setup viewed from the user-side of the wind tunnel. Detail of PIV recording area and model wind turbine in figure 2.4. Inflow parameters  $u_*$ ,  $\Delta U^+$ , and  $y_0$  are related through equation 2.2. The schematic above is for reference only, dimensions are not to scale.

via stereographic particle image velocimetry (SPIV). The same relative positioning of SPIV windows were made around the exit row of wind turbines.

## 2.2 Inflow Conditioning

The wind tunnel is furnished with a passive grid at the entrance of the test section to introduce turbulence. The grid consists of 7 horizontal and 6 vertical rods and was placed far enough upstream of the test models to ensure that the flow turbulence was in homogenous decay before reaching the first measurement locations.

Removable vertical strakes were fabricated to further modify the inflow of the wind tunnel. The use of vertical strakes has been common practice in wind tunnel experiments in simulating the atmospheric boundary layer. The specific shapes and profiles used have varied with application but has been fairly well diagnosed since the 1970's [14, 16]. These strakes are composed of 0.0125 m thick plexiglass and shaped to precondition the boundary layer to more closely match observed trends in the atmospheric boundary layer. There were 9 vertical strakes spaced 0.136 m apart across the width of the tunnel. The strakes were 0.5 m downstream of the active grid.

As a final conditioning element for the inflow of the experiment, semi-porous surface roughness was added to the floor of the wind tunnel via small-diameter chains. The chains have an average diameter of approximately 0.0075 m. The introduction of surface roughness to the boundary layer extends the influence of the high shear zone as seen in the ABL. This modifies the general profile of the inflow to match those shown in §2.2.1 below.

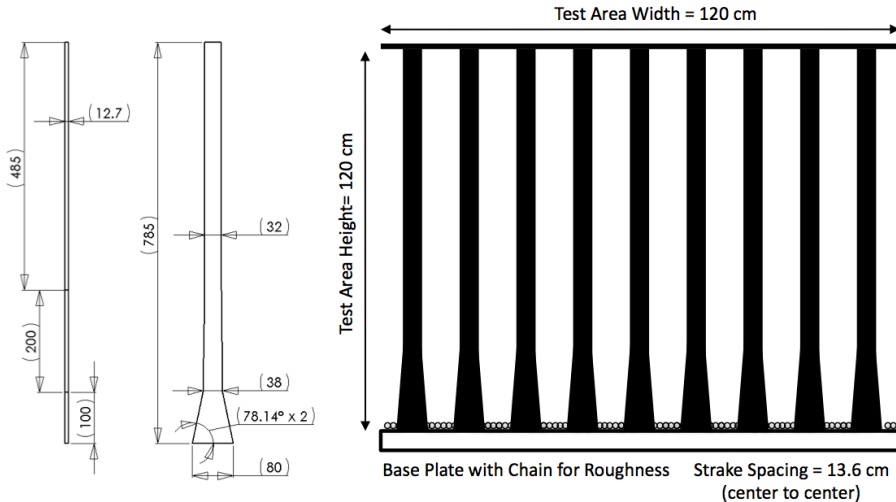


Figure 2.2: Schematic of vertical stakes used to generate mean shear flow. Stakes were designed to simulate the atmospheric boundary layer typical of wind farms. Dimensions in detail subfigure (left) are all in mm.

### 2.2.1 Inflow characterization

Wind turbines operate in the atmospheric boundary layer (ABL) rather than standard flat plate boundary layers where the law of the wall is properly applied. The wind tunnel ABL that is characterized with three parameters: an effective roughness scale, the friction velocity, and a boundary layer velocity deficit. The friction velocity is typically calculated as a product of the wall-normal velocity gradient evaluated at the wall and the kinematic viscosity according to,

$$u_\tau = \sqrt{\frac{\tau_w}{\rho}} \quad \text{with} \quad \tau_w = \mu \frac{\partial U}{\partial y} \Big|_{y=0} \quad (2.1)$$

However, as is often the case in wind turbine studies in the ABL, measurements are not made at the level of the ground and the velocity gradient cannot be directly assessed in that location. Instead the friction velocity is evaluated as  $u_* = \sqrt{-\overline{u'v'}}$  in the constant shear layer, where  $\frac{\partial}{\partial y}(-\overline{u'v'}) = 0$  (in the log layer the boundary region). The subscript change from  $\tau$  to  $*$  indicates that this is an effective value of the friction velocity rather than that according to the classical definition. Defining a velocity deficit,  $\Delta U^+$ , and effective surface roughness,  $y_0$ , one can use the relationship

$$\Delta U^+ = B + \frac{1}{\kappa} \ln \left( \frac{u_* y_0}{\nu} \right) \quad (2.2)$$

in the log layer of the ABL. In equation 2.2,  $B = 5.5$  and the von Kármán constant is

taken as,  $\kappa \approx 0.4$ . With these parameters, one may write

$$\tilde{u}(y) = u_* \left( \frac{1}{\kappa} \ln \left( \frac{u_* y}{\nu} \right) + B - \Delta U^+ \right) \quad (2.3)$$

Equation 2.3 is fit to the mean streamwise velocity profile upstream of the wind turbine farm. Parameters the data fit are shown in figure 2.3.

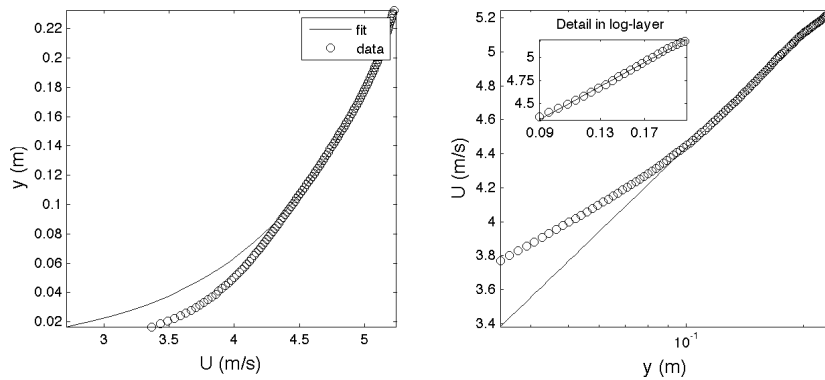


Figure 2.3: Inflow of the ABL to the turbine array in linear (left) and logscale (right) units. A fit line was generated according to equation 2.1 in the log layer (specifically,  $y$  varies from 0.108 m to 0.233 m). The effective friction velocity,  $u_*$  was calculated to be 0.385 m/s and the effective roughness  $10^{-4}$  m. This lead to a velocity deficit of  $\Delta U^+ = 14.9$  m/s.

## 2.3 Flow measurement system

The stereographic Particle Image Velocimetry (SPIV) data in this experiment was collected in two windows simultaneously as shown in figure 2.4. Data was collected for windows directly upstream and directly downstream of the entrance and outlet turbines in the array. The SPIV was comprised of a *LaVision* system consisting of an Nd:Yag (532 nm, 1200 mJ, 4 ns duration) pulsed laser and four CCD cameras arranged in pairs for the two SPIV windows. The flow was seeded with neutrally buoyant fluid particles of diethylhexyl sebacate and allowed to mix thoroughly. Seeding was kept at a constant level throughout experimentation to ensure resolution of data and reduce spurious vector generation. The laser sheet was approximately 0.001 m thick with a divergence angle of less than 5 mrad across the span of measurement locations shown in figures 2.1 and 2.4. A single laser sheet was used for both measurement locations and was blocked in the center to reduce reflections from the turbine assemblies.

The raw images were processed into vector fields using a multi-pass FFT based correlation algorithm of reducing size interrogation windows (twice each at  $64 \times 64$  and  $32 \times 32$  pixels) with a 50% overlap. Vector fields were then flagged and filtered with a combination of algorithms to identify and omit erroneous measurements from the calculations of statistics. The algorithms used both extreme value limits and interpolations to replace vectors exceeding typical deviations from neighboring locations.

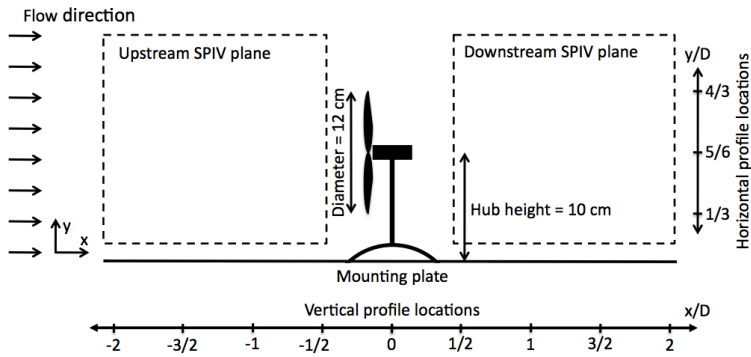


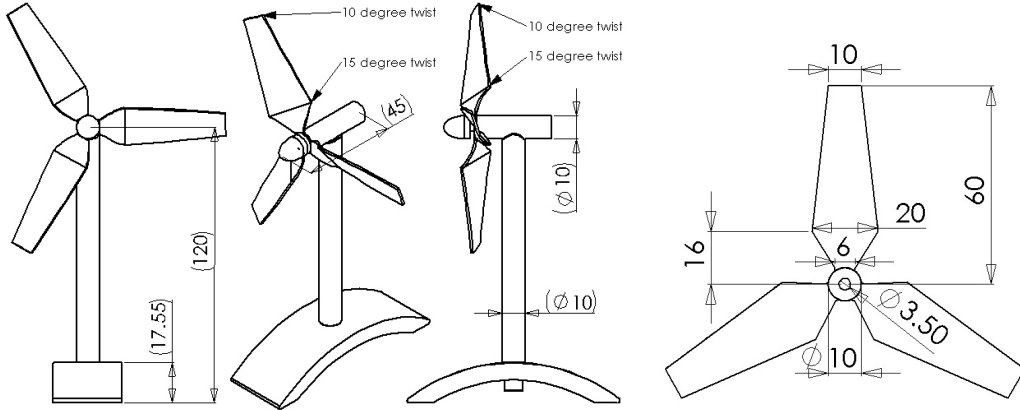
Figure 2.4: Side view of wind turbine model showing the relative location of SPIV planes and profile locations. Profiles and contour plots shown in Chapter 4.

## 2.4 Wind turbine models

The turbine models were fabricated in-house according to a design specified to meet typical tip-speed ratios found in full-scale turbine arrays. The rotor blades were laser cut out of 0.0005 m thick steel sheet and formed to shape using a positive/negative die press to ensure uniformity. The die press was designed in-house using Solidworks 3D CAD software and set each of the rotor blades to a pitch of  $15^\circ$  from the plane of the rotor and a  $5^\circ$  twist from root to tip.

The nacelle of each turbine consisted of an electric motor (Faulhaber GMBH & Co Series 1331T012SR) acting as a generator mounted to a 0.01 m hollow steel shaft. The motors were cylindrical with an outside diameter of 0.013 m and a nominal operating voltage of 12 V and a no-load current of 0.0105 A. The motors were aligned with the flow with the shaft pointed upstream. The mast was cylindrical in geometry and the hollow interior allowed for electrical wiring for the motor/generator and the torque system (detailed below) to be removed from the flow. Figure 2.5 shows schematics of the fully assembled turbine models including mast, nacelle, rotor, mounting plate, and a detail

view of the rotor before blade twisting.



(a) Perspective views of wind turbine models used in experiments.  
(b) Detail of rotor model before addition of blade twist.

Figure 2.5: Technical drawing of model wind turbines used in experiments. The rotor blades were designed such that the widest part was pitched to  $15^\circ$  from the plane of the hub. The tips of each blade were pitched to  $10^\circ$  from the plane of the hub. All dimensions are in millimeters. Note that the mounting plate shown in 2.5(a) spans the full width of the wind tunnel and only a small section is shown.

## 2.5 Torque sensing system

The torque sensing system implemented in the experiment here followed the design and procedure outlined in [26] in which a housing was built to hold the electric motor described above such that it was free to rotate along its operating axis. The motor acting as a generator was supported in a solid metal housing by two identical VXB ball bearings aligned concentrically with the shaft of the generator. The inner and outer diameters of the bearings were 0.013 m and 0.024 m respectively, and the outer diameter of the housing was approximately 0.0254 m. The bearings allowed the entire generator to freely rotate in reaction to the application of torque to its shaft. On the back (downstream) side of the motor/bearing housing a pressing arm with a pin was attached such that any applied torque resulted in the flexure of a sensitive bending plate consisting of a 0.0025 m wide strip of 0.0005 m thick bronze 0.02 m in length. To the bronze strip were mounted two small  $120 \Omega$  linear strain gauges (OMEGA SGD-3/120-LY11) that measured the torque required to keep the motor at the same relative alignment in the tunnel. Figure 2.6(a) shows the assembly of the motor/bearing housing labeling the important components.

The two strain signals from the flexure of the bending arm was measured with a Wheatstone bridge constructed with four  $120\ \Omega$  linear strain gages. The two resistors not fixed to the flexure arm required to form a complete bridge came from strain gauges of the same type mounted to a  $0.10 \times 0.1$  m aluminum cube. The entire strain-gauge/bridge system was conditioned and amplified by an external electrical module (OMEGA DMD-465 Bridgesensor) and measured at 10 kHz via LabVIEW and a National Instruments DAQ.

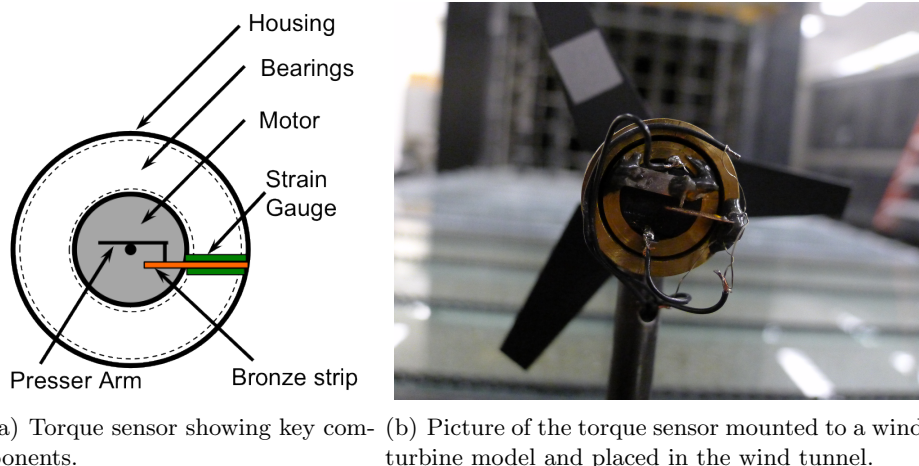


Figure 2.6: Schematic, 2.6(a), and picture, 2.6(b), of the torque sensor used in the experiment. The reflective tape show in the top rotor blade in 2.6(b) was used in the optical measurements of angular velocity.

Tip speeds were monitored through an optical tracker and controlled by applying resistive electrical loads to the motors. Each row of turbine models was set to operate under loading conditions corresponding to the peaks of their power curves. The masts were hollow allowing electrical wiring for speed control and other measurements to be contained and out of the mean flow mitigating added effects in the main wake area.

## 2.6 Test Cases

Several configurations of the wind turbine array were tested successively in the wind tunnel. The data here correspond to a comparison of the base case (a four by three rectangular arrangement) and two different row-offset arrangements. Streamwise spacing of rows and spanwise spacing of turbines (within each row) remained constant for each configuration. An overhead view of each configuration can be seen in figure 2.7. Note that the two offset cases use the same arrangement scheme with a spanwise shift

to test the wakes and performance of turbines in different positions within the array.

Figure 2.4 depicts an example turbine model used in the experiments. All turbine models were of the same dimensions and used the identical mounting plates with positioning markers to achieve the configurations shown in figure 2.7. All of the data collected for the test cases described here were collected under controlled conditions. The wind tunnel settings were such that the free-stream velocity was held at a constant 6.5 m/s upstream of the turbine array. For all cases, temperature was fixed at approximately 23° C and the ABL simulated by the tunnel was in neutrally stratified conditions.

## 2.7 Data Sets and Convergence

According to *Lectures in Turbulence for the 21st Century* [21] the variability,  $\epsilon(u(\mathbf{x}))$ , of measurements made on a stationary random process is defined as,

$$\epsilon(u(\mathbf{x})) = \left( \frac{1}{N_{eff}} \frac{(\tilde{u}(\mathbf{x}) - U(\mathbf{x}))^2}{U^2(\mathbf{x})} \right)^{\frac{1}{2}} \quad (2.4)$$

and can be viewed as one measure of the convergence of the statistics regarding flow measurements. In the equation  $N_{eff}$  is the effective number of measurements at each point.

For the experiment outline above, measurements were taken simultaneously in locations immediately upstream and downstream of the turbine locations in question. The convergence test of the data sets was run for sets of all 2000, 1500, and 1000 independent measurements. Table 2.1 shows the resulting values of the variability as delineated by equation 2.4. Because PIV is a field measurement system, the variability can be separately defined for each position in the measurement field. Areas subject to stronger fluctuations of velocity or turbulence intensity, such as immediately downstream of the nacelle, will exhibit greater variability than areas of consisted flow velocity, such as locations above the turbine canopy. Table 2.1 shows maximum and minimum values of  $\epsilon(u)$  corresponding to the SPIV window directly upstream of the entrance row turbine in the basic arrangement.

An analogous test was applied to the fluctuations only. In this test, the convergence of the variance was tested according to the same scheme outlined above. The fluctuations

Table 2.1: Relative error convergence of measurements based on size of data set.

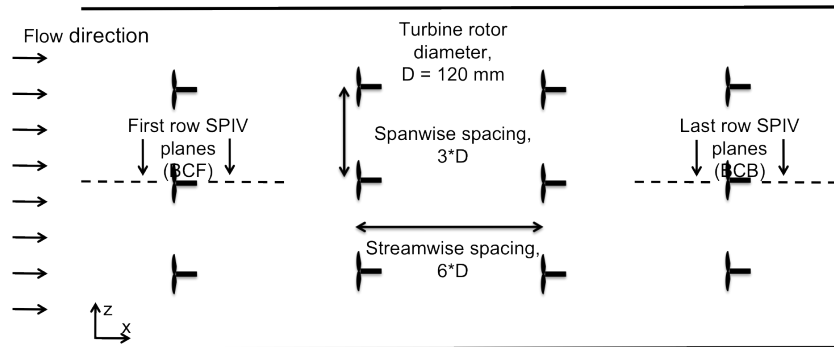
Set size	$\epsilon_{min}(\tilde{u}(\mathbf{x}))$	$\epsilon_{max}(\tilde{u}(\mathbf{x}))$	$\epsilon_{mean}(\tilde{u}(\mathbf{x}))$
2000	0.0014	0.0069	0.0022
1500	0.0016	0.0078	0.0026
1000	0.0020	0.0093	0.0031

are expected to converge much slower than the instantaneous flow above. Table 2.2 shows the results of the second convergence test.

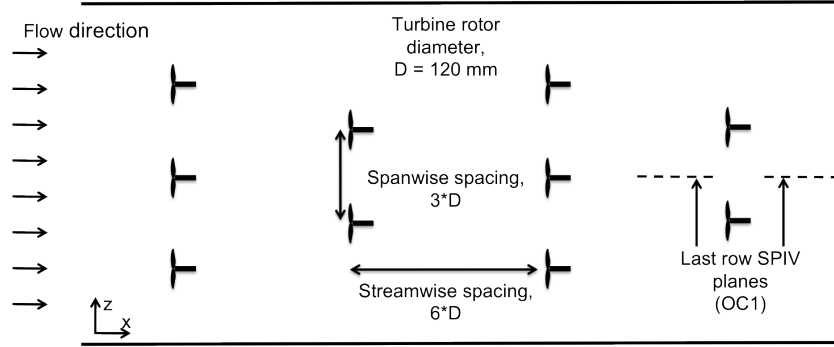
Table 2.2: Relative error convergence of fluctuating velocities based on size of data set.

Set size	$\epsilon_{min}(u(\mathbf{x}))$	$\epsilon_{max}(u(\mathbf{x}))$	$\epsilon_{mean}(u(\mathbf{x}))$
2000	0.0381	0.1925	0.0744
1500	0.0383	0.1932	0.0751
1000	0.0391	0.2478	0.0757

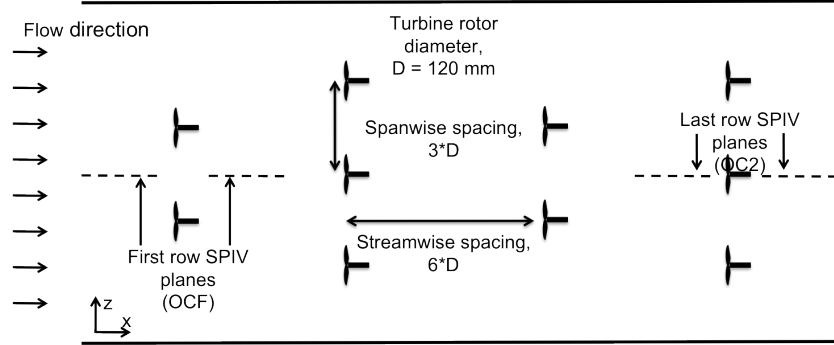
The convergence tests applied here shows data sets of 2000 independent measurements within the initial bounds of  $\epsilon_{mean}(u(\mathbf{x})) < 0.0025$  or average error at any measurement point is less than 0.25%. It can also be concluded that the average variability of the variance has converged to less than 7.5%.



(a) Schematic of the base wind turbine configuration



(b) Schematic of the first offset wind turbine configuration



(c) Schematic of the second offset wind turbine configuration

Figure 2.7: In all cases, the downstream spacing is equivalent to six times the rotor diameter (0.72 m). The spanwise spacing is three rotor diameters (0.36 m). SPIV planes in subfigures 2.7(a), 2.7(b), and 2.7(c) correspond to the locations of contours described in Chapter 4 and table 4.1.

## Chapter 3

# Results of Power Measurements

To ensure accurate measurements of torque and power, the strain gauges used in the torque sensors were subjected to calibration before collection of data in each measurement location. Calibration of strain gauges was according to manufacturer specifications by applying a static load between 0.2 g and 5.5 g to the bronze armature fixed to the sensor. These calibration curves were used to correct data from the dynamic loading of the strain gauges acquired in experiments. An example of the strain gauge calibration is shown in figure 3.1.

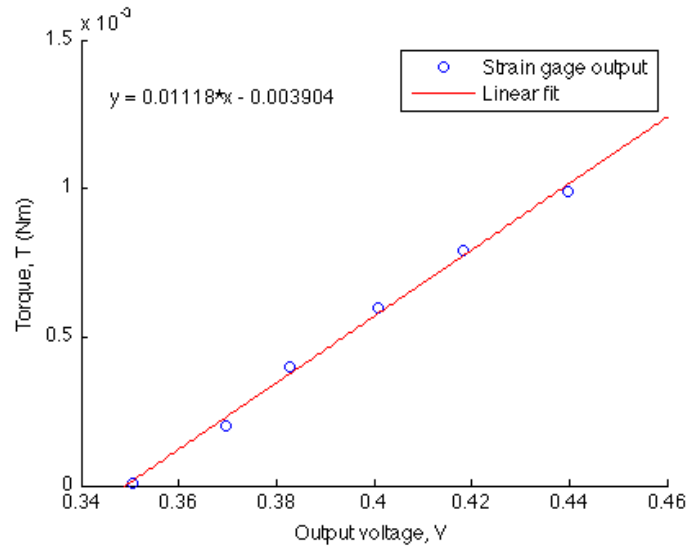


Figure 3.1: Example strain gauge calibration curve. Curve shown corresponds to the entrance row turbine in the offset arrangement.

Measurements were made of the resistive load of the circuits containing the turbine models and their rates of rotation according to §2. The loading in the experiment was

tuned to the design specifications of the electric motors comprising the nacelles of the turbine models. Loads varied from  $2 \Omega$  to  $10 k\Omega$ .

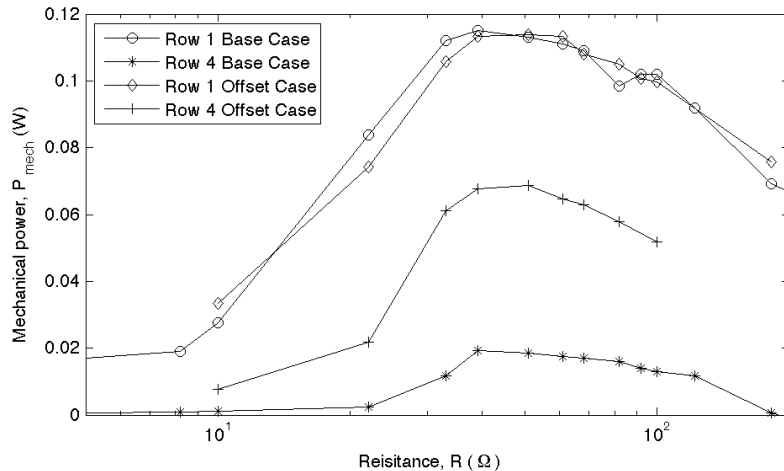


Figure 3.2: Power curves generated by the entrance and exit row wind turbine models. Power measurements for both offset cases are included. The entrance row of the offset data (+) corresponds to the (3-2-3-2) configuration and the exit row (\*) corresponds to the (2-3-2-3) configuration.

The output of the power measurements shown in figure 3.2 show clearly the difference of turbine performance according to configuration. The entrance row turbines produced nearly identical power curves in all configurations. For clarity, only one power curve corresponding to the offset arrangements is shown in the figure.

The most salient point provided by figure 3.2 is that the exit row for the offset arrangement shows a peak that is more than three times greater than in the base case. This increase in power is due to the increase of spacing from 6 rotor diameters to 12 as shown in figure 2.7. Further power measurements were made for the interior rows of turbines but have been omitted from the present study as the SPIV data in Chapter 4 and the results of the POD in Chapter 5 focuses only on entrance and exit rows. In both variations of the offset arrangement, the second row turbines perform nearly as well as the entrance row, as expected, as there are no direct upstream obstructions and they receive the undisturbed ABL as inflow. Power is discussed as it relates to the POD modes more in Chapter 5

Curves of the power coefficient  $c_p$  according to tip speed ratio  $\lambda_{tsr}$  are shown in figure 3.3. According to the figure, the offset case out-performed the base arrangement for both the entrance and exit rows wind turbine models. The entrance row of both arrangements show the peak value of  $c_p$  occurring at  $\lambda_{tsr} \approx 3$ . The peak of the exit

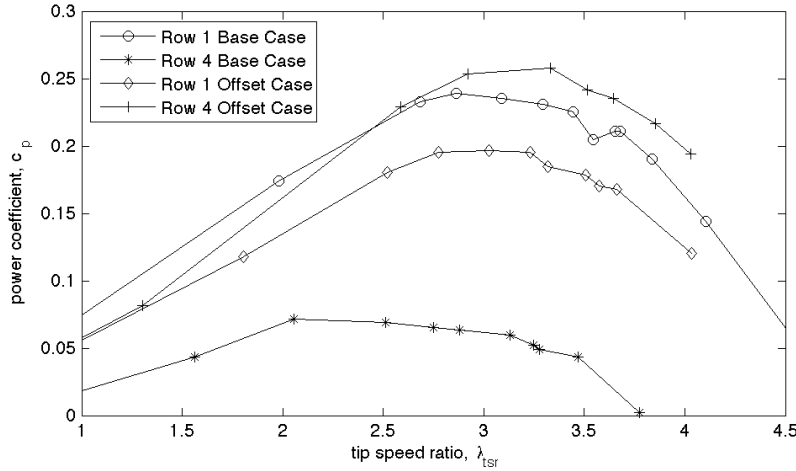


Figure 3.3: Curves of power coefficient  $c_p$  by tip speed ratio  $\lambda_{tsr}$  according to equations 1.11 and 1.12, respectively. The exit row turbine performance shows a five-fold improvement from the base arrangement to the offset arrangement.

row of the offset case shows a peak closer to  $\lambda_{tsr} = 3.5$ . Velocity measurements used in calculating  $\bar{u}_1$  are shown in Chapter 4

Other studies have shown values of  $c_p$  on the order of 0.4 to 0.5. The curves of  $c_p$  here show lower maximum values than expected, which indicates that either there are increased mechanical losses in the torque sensing device or that the rotor blade design could be further improved. In this experiment, the rotor blades are not airfoils but shaped sheet metal; meaning that the blades are drag driven rather than lift driven like wind turbine blades in use in most turbine arrays. An improvement in blade design to incorporate airfoil dynamics and make the turbine a lift-driven device would improve the maximum values of  $c_p$ .



# Chapter 4

## Results of SPIV

Many of the data and figures presented in this Chapter display data in three formats described below. All data displayed and discussed corresponds to either the basic configuration, either for the front row (BCF) or the back row (BCB), the first offset case (OC1) or the second offset case either for the front row (OCF) or the back row (OC2). This naming scheme is adopted in the following sections for brevity. The locations of these SPIV windows are delineated in the experimental schematics shown in figure 2.7. The locations of data in contour plots are named in table 4.1. Many of the figures in this chapter conform to one of the following three forms, outlined here for reference:

- **Horizontal profiles:** in which profiles of the quantity in question are drawn at specific distances in the wall-normal direction. Specifically profiles are drawn at the bottom tip of the rotor, at the turbine hub height, and the top tip of the rotor. In normalized coordinates these locations are,  $y/D \in [\frac{1}{2}, 1, \frac{3}{2}]$ .
- **Vertical profiles:** profiles of the quantity in question are calculated in the wall-normal direction at specific values of  $x/D$  with respect to the specific turbine location. Specifically,  $x/D \in [-2, -\frac{3}{2}, -1, -\frac{1}{2}, \frac{1}{2}, 1, \frac{3}{2}, 2]$ .
- **Contour plots:** averages of the quantity in question shown for each SPIV plane. Table 4.1 shows the positions and names of each SPIV window in the contour planes. The blank spaces in table 4.1 are the upstream positions of the first offset configuration. Because these positions are statistically identical to BCF, they have been omitted from the analysis for clarity.

Table 4.1: Presentation of SPIV planes in all contour figures.

Front row upstream	Front row downstream	Back row upstream	Back row downstream
BCF	BCF	BCB	BCB
		OC1	OC1
OCF	OCF	OC2	OC2

The following sections (§4.1 through §4.5) provide a cursory review of the analysis results. By design of the experiments, the SPIV window upstream of the front row turbines should be statistically identical for all configurations of the array except in the region very near ( $x/D > -1.25$ ) a turbine model. In OCF, where there is no turbine, the upstream SPIV plane shows the development of the undisturbed ABL. For this reason, this window is used to determine to what degree the flow has recovered to its natural state and to determine the deficit of energy in the wakes. The downstream position of OCF, however, includes effects of the mounting plate for the turbines.

## 4.1 Flow upstream of turbines

Looking first at the contours of mean streamwise velocity,  $U$ , in figure 4.1 one observes the similarity between the inflow fields of BCF and OCF, as expected. In both cases, there are no upstream obstructions that could influence the shape and dynamics of the ABL. In the other cases (BCB, OC1, and OC2) the inflow fields are just upstream of the exit row of turbines in the array. In each of these cases the ABL is in various degrees of recovery to its “natural” state.

Seen in the contours of BCF and OCF, there is a small difference in close proximity ( $x/D > -1.25$ ) to the turbine hub. In BCF one can see a reduction in the mean streamwise velocity due to blockage of the flow. This blockage in  $U$  results in an acceleration of the flow in the wall-normal and spanwise directions thus one can also observe in figure 4.2 a spreading of the flow around the turbine for BCF. Recalling that the inflow for OCF is essentially the undisturbed ABL, one observes  $V$  in the range from  $-0.05$  to  $0.15$  m/s. In comparison, the extreme values of  $V$  in the upstream section of BCF are on the order of  $0.35$  m/s near the top tip of the rotor and  $-0.1$  m/s near the bottom tip of the rotor.

Looking at the inflow planes for the exit row turbine position (BCB, OC1, and OC2) the same blockage effect and vertical acceleration is visible wherever a turbine is present. In OC1, there is no turbine and the field shows the mid- and far-wake ( $4 < x/D < 8$ )

recovery of the third row turbine. In all three of the exit row SPIV planes, the the mean profiles of  $U$  are decreased as the ABL is not yet recovered to its natural state. Where a turbine is present, the spreading effect viewed in  $V$  is approximately 15 – 30 % less intense than in the entrance row. This decrease in extrema in  $V$  is clearly visible in both the horizontal profiles (figures 4.3 and 4.4) and the vertical profiles (figure 4.5).

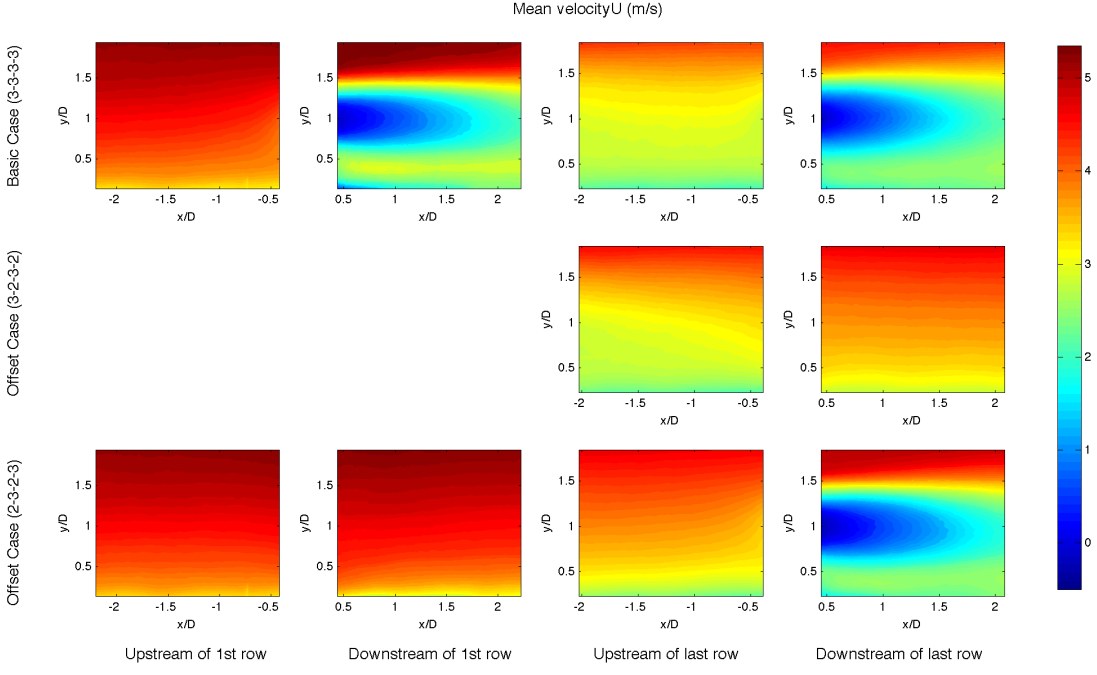


Figure 4.1: Contours of mean velocity in the streamwise direction,  $U$ .

## 4.2 Wake comparisons

Immediately visible in figures 4.1 and 4.5(a) one can see the wake areas behind in the SPIV planes downstream of the wind turbines. The three wakes occur in BCF, BCB, and OC2. As discussed above, profiles and contours for the entrance row turbines in the (3-2-3-2) offset arrangement are nearly identical to BCF and have been omitted from all figures for clarity.

Comparing the size and intensity of the three wakes in figure 4.1 and described above, BCF shows the greatest mean flow energy deficit in  $U$  from the undisturbed ABL. The immediate implication of this is that BCF extracts the most energy from the wind. The energy available to each successive row of turbines in the array depends on the recovery of the ABL between turbine rows. Thus we expect to see a smaller range of

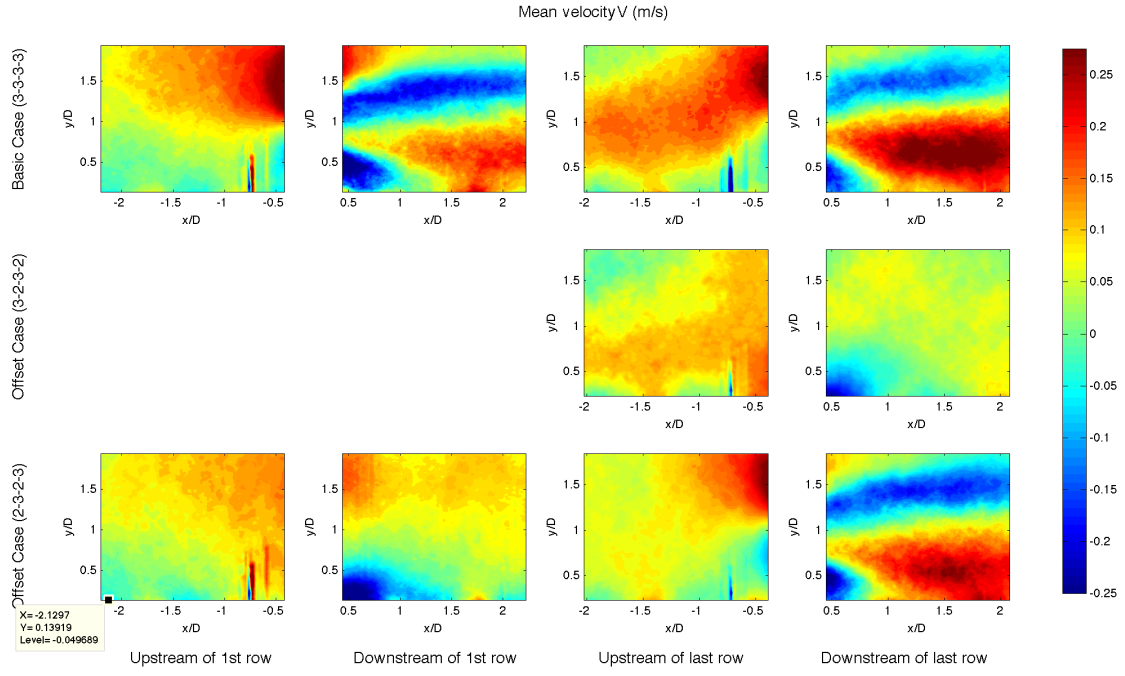


Figure 4.2: Contours of mean velocity in the wall-normal direction,  $V$ .

dynamics in the wakes of BCB and OC2. This is confirmed by power curves generated for the entrance and exit rows in the different array configurations as seen in figures 3.2 and 3.3.

Figures 4.3 and 4.5(a) reflect the reduced range of dynamics as well. Comparing the vertical profiles in the wakes of BCF, BCB, and OC2, we see that the three wakes are nearly equal in intensity and that the mean streamwise velocity varies from  $U = 5.5$  m/s (slightly less than that of the freestream), to a strong recirculation region behind the nacelle where  $U = -0.45$  m/s at  $x/D = 0.5$ . In the exit row of turbines, one can observe that the wakes reach a extreme recirculation velocity on the same order as the first row turbines but the inflow velocity in the exit rows are reduced.

The blockage effect mentioned briefly in §4.1 can be seen in the upstream edge of the SPIV windows containing the wakes (seen especially in the vertical profiles at  $x/D = -0.5$ ). This is rapidly overshadowed with the mixing effect produced by the turbines. The extreme values of the wall-normal velocity,  $V$ , are reached in the area of  $x/D = 1.0$ . Specifically, the wall-normal velocity in the wake regions of BCF range from  $V = -0.15$  m/s to  $V = 0.35$  m/s.

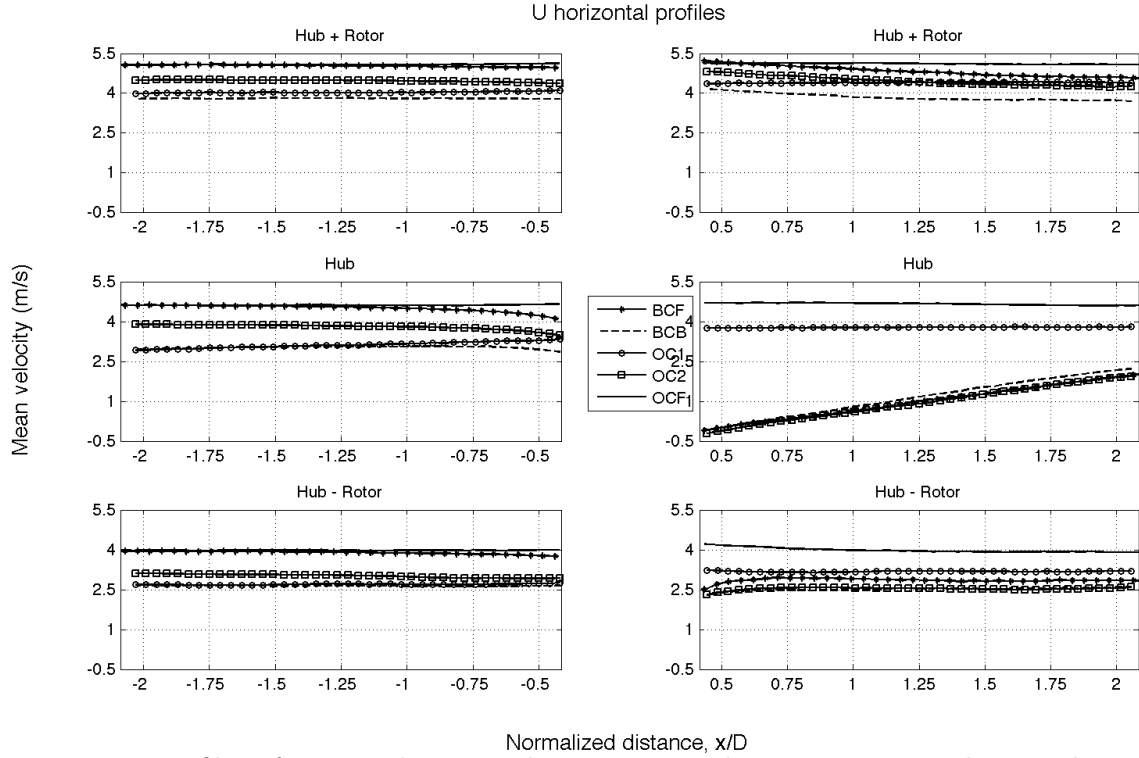


Figure 4.3: Profiles of mean velocity in the streamwise direction,  $U$ , according to the streamwise coordinate. Profiles shown correspond to the hub of the rotor  $\pm$  the radius of the rotor.

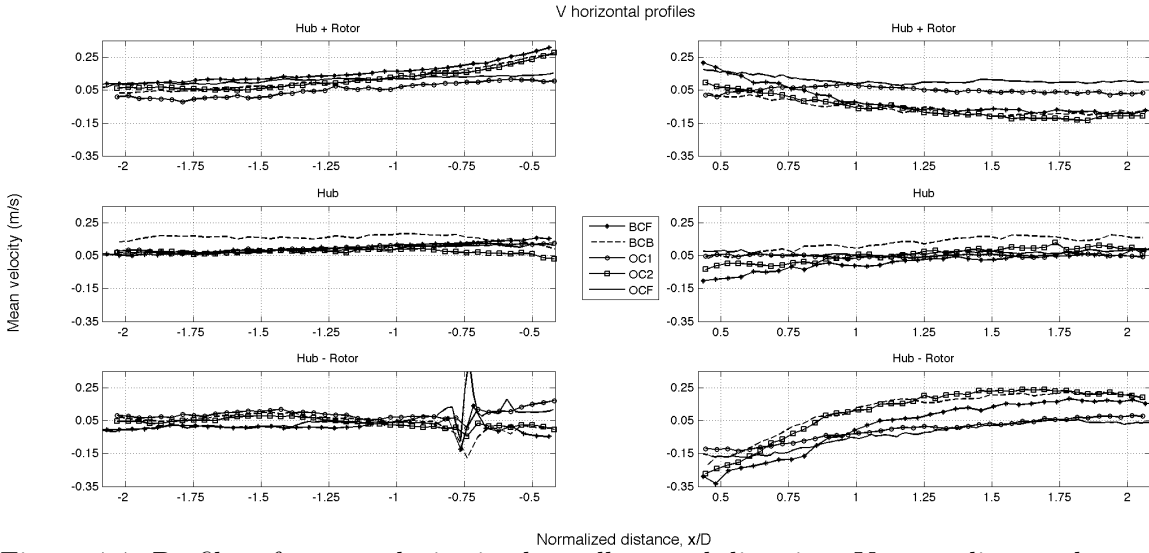


Figure 4.4: Profiles of mean velocity in the wall-normal direction,  $V$ , according to the streamwise coordinate. Profiles shown correspond to the hub of the rotor  $\pm$  the radius of the rotor.

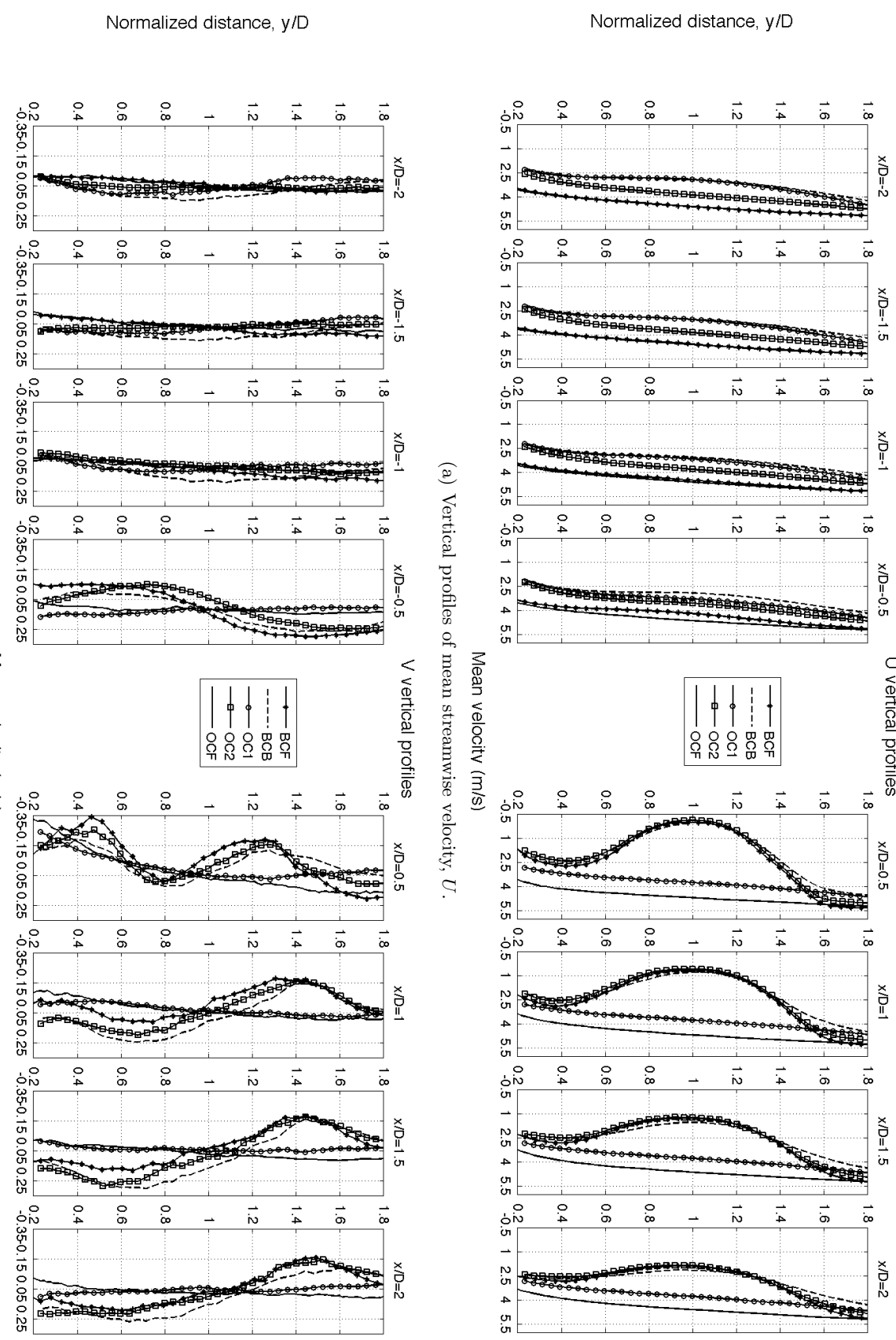


Figure 4.5: Profiles of mean velocity in streamwise 4.5(a) and wall-normal 4.5(b) directions according to the wall-normal coordinate. Profiles are taken at half-diameter distances ( $x/D = \pm 0.5 \times n, n \in [1, 2, 3, 4]$ ) upstream and downstream of wind turbine model.

The spanwise velocity,  $W$  (the out of plane component here), shows similar behavior as  $V$  but at reduced magnitude. Interesting to note in figure 4.6 is that the entrance row turbine located in BCF shows *less* extreme values of  $W$  as the back row cases, BCB and OC2. As with the other components of mean velocity,  $W$  can be seen acting in the far wake as the upstream windows to the exit row locations. Note that in figure 4.6 the upstream windows of BCB and OC2,  $W$  is nearly null everywhere and that the blockage effect seen in  $U$  and  $V$  is not present.

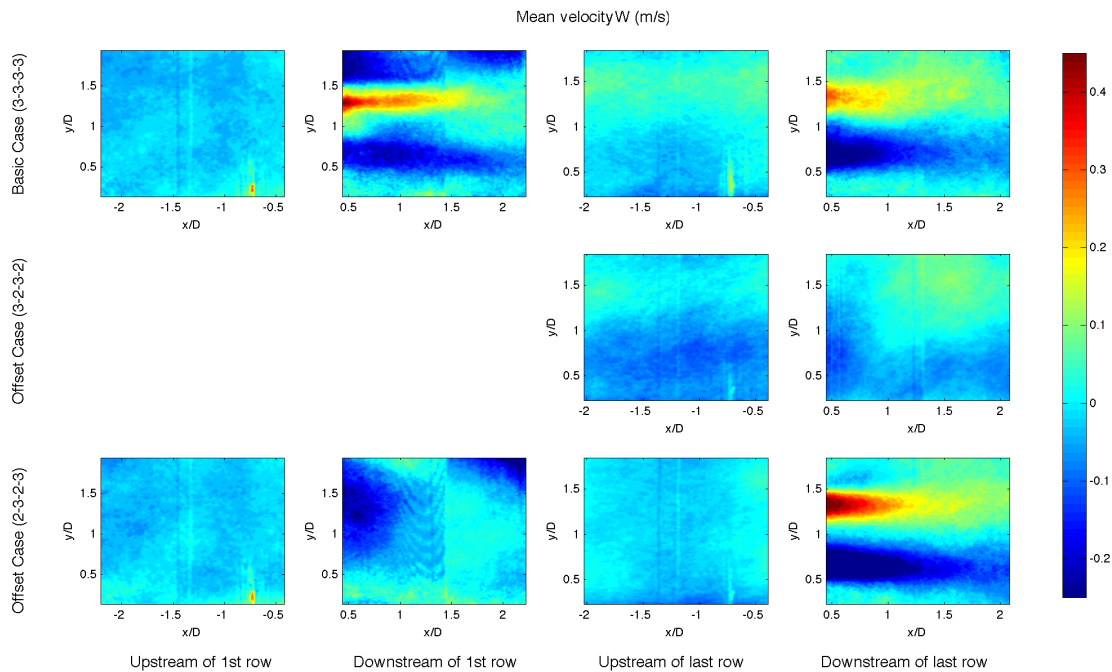


Figure 4.6: Contour plots of spanwise velocity component,  $W$ . Distinctive wake behavior shown in greater clarity in wakes following more organized inflows (BCF in the top-left and OC2 in the bottom-right).

Because the spanwise component of velocity is the smallest in magnitude (by at least one order) and that the measurement plane is aligned with the  $x - y$  plane in the tunnel, the fluctuations and stresses containing  $w$  are not as converged as the other components. Stresses including  $w$  have been omitted from sections §4.3 through §4.5 for clarity with the exception of the turbulent kinetic energy.

### 4.3 Reynolds stresses comparisons

The Reynolds stress tensor appears in the mean momentum equation as  $\tau_{ij} = \overline{u'_i u'_j}$ , the ensemble average of fluctuations of velocity components at any particular location.

Where  $\overline{u'_i u'_j}$  is a second-order symmetrical tensor.

The trace elements of the shear stress tensor  $\tau_{ij}$  are the Reynolds normal stresses and are the contributors to the turbulent kinetic energy discussed below. Figures 4.7 and 4.8 show the contour plots of the Reynolds normal stresses in the same configuration as above.

As seen in the figures depicting  $U$  the entrance row of the offset case, OCF, shows activity in the ABL without added behavior and structures due to the presence of wind turbines. The wake region of the entrance row of the base configuration, BCF, shows the strongest Reynolds normal stresses associated with the turbine mast, where the intensity of  $\overline{u^2}$  reaches approximately  $1.0 \text{ m}^2/\text{s}^2$ . BCF also shows a large region of activity following the top tip of the rotor disc. However, when looking at the exit row turbines, one can observe the effect of an accumulation of turbulence in the wakes of BCB and OC2 where the local maxima are on the order of  $\overline{u^2} = 1.35 \text{ m}^2/\text{s}^2$ , some 20% greater than in entrance turbine wakes.

Figure 4.8 shows the  $\overline{v^2}$  component of  $\tau_{ij}$ . In all cases, the greatest intensity of  $\overline{v^2}$  is directly behind the turbine at hub height. One important note in figure 4.8 is the low intensity region above the nacelle of the turbine but inside the radius of the rotor in the very near wake ( $0.5 < x/d < 1$ ). In this region, the rotor blades induce strong variations in streamwise directionw but not in the wall-normal sense. Tip vortices are evidenced in the contour plots and also in the vertical profiles 4.11(b) as a local maximum at  $y/D \approx 1.5$ . In an average sense, the local maximum of the tip vortices is quickly overshadowed by the recirculation behind the nacelle. As  $x/D$  increases tip vortices disappear from profiles and contour plots of  $\overline{v^2}$  (also seen in  $-\overline{uv}$ , below).

The far wake is visible as the upstream SPIV window for the exit row in all cases. In the base case (top row of contour plots) the far wake ( $4 < x/D < 6$ ) of the third row of turbines is visible. The same is true for OC1 (middle row of contour plots) with the difference that the entrance row turbine wake has had twice as long to recover to the undisturbed ABL before the third row of turbines. OC2, however, shows an significant difference from the other two, representing the recovery of the wake from  $x/D = 10$  to  $x/D = 12$ .

From the Reynolds normal stresses the turbulent kinetic energy is calculated as  $k = \frac{1}{2}(\overline{u^2} + \overline{v^2} + \overline{w'^2})$  as in equation 1.4 from Chapter 1. This quantity provides an estimation of the energy transferred from the mean flow into turbulence by the presence

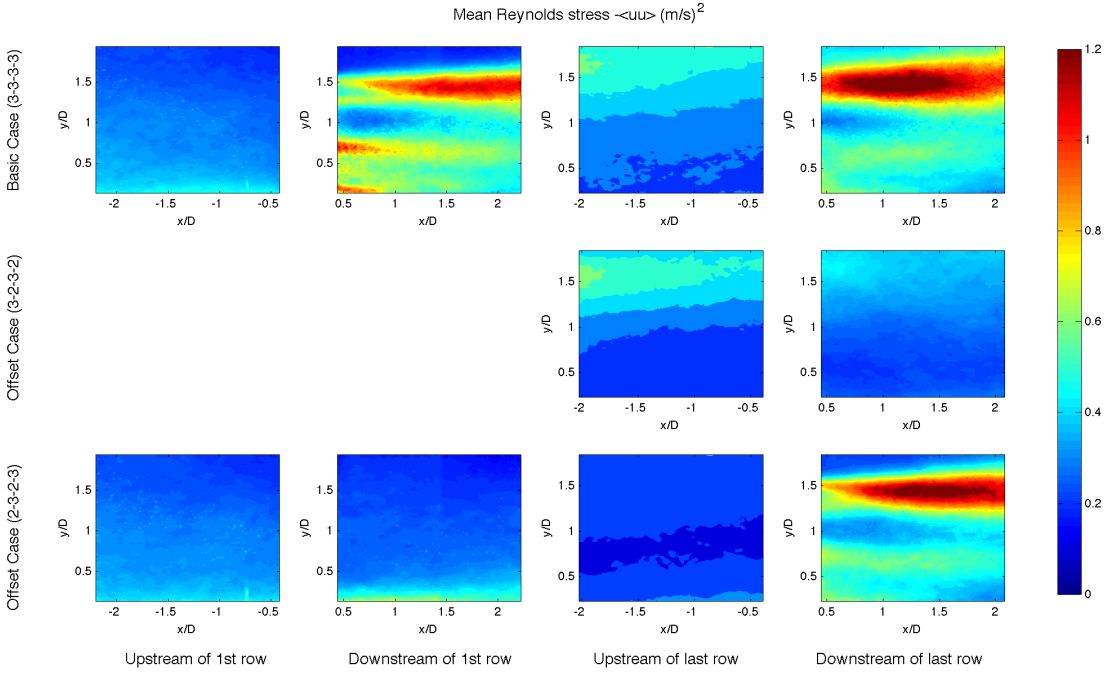


Figure 4.7: Contour plots of  $\overline{u^2}$  for all SPIV locations as delineated in figure 2.7 and by table 4.1.

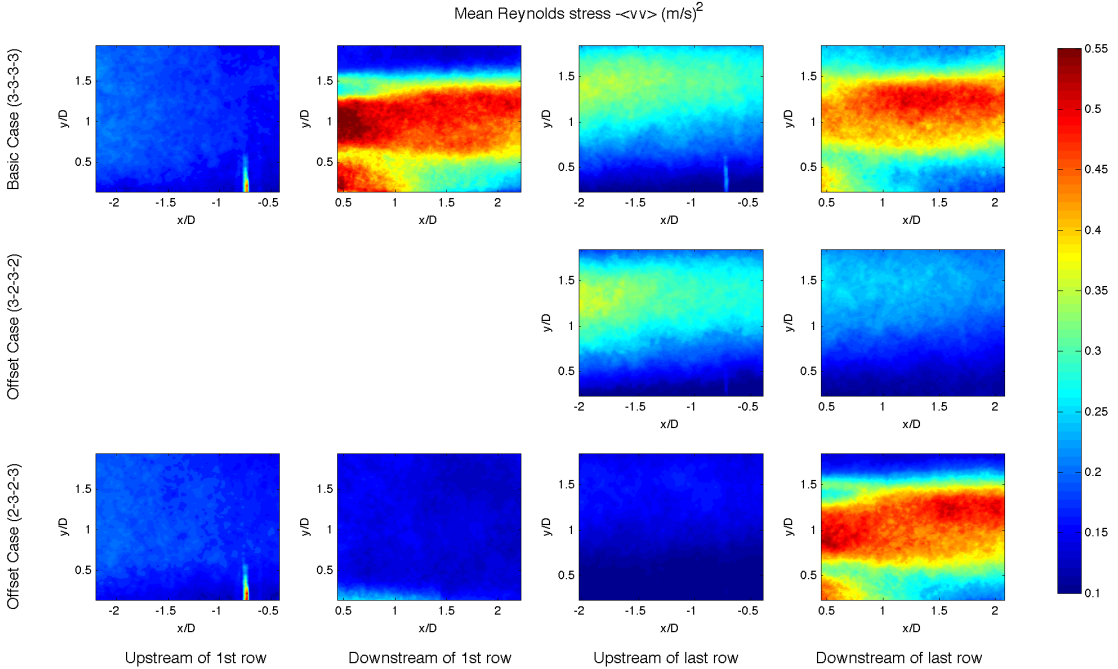


Figure 4.8: Contour plots of  $\overline{v^2}$  for all SPIV locations as delineated in figure 2.7 and by table 4.1.

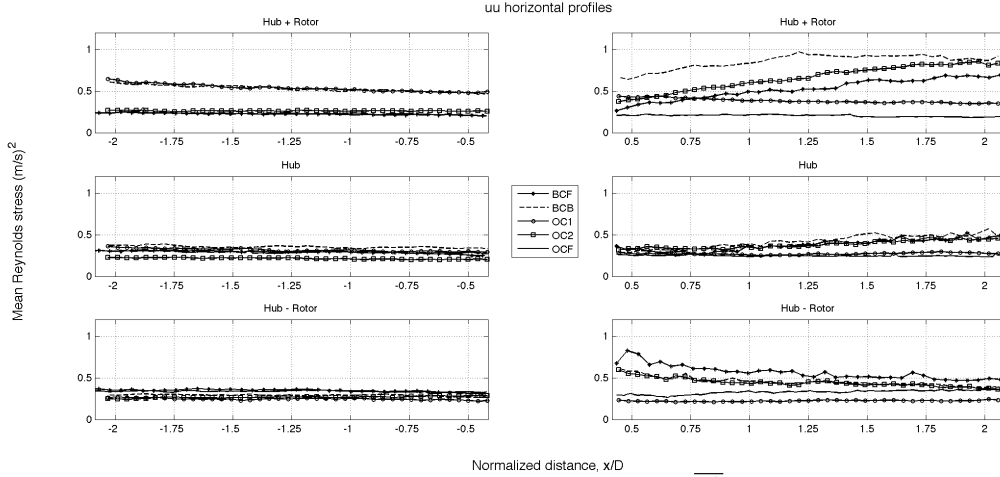


Figure 4.9: Profiles of streamwise normal Reynolds stress,  $\overline{u^2}$  according to the streamwise coordinate. Profiles shown correspond to the hub of the rotor  $\pm$  the radius of the rotor.

and forcing of the turbines. As seen in many of the above figures and contours, the turbulent kinetic energy is strongly affected by disturbances to the ABL. The wakes are clearly present with contributions coming mostly from the components  $\overline{u^2}$  and  $\overline{v^2}$ . As expected, the contribution to  $k$  from the spanwise Reynolds stress is on the order of 80% less than from the other components. Figure 4.14(a) shows vertical profiles of the turbulent kinetic energy.

Again, the wake regions are clearly identified in all contours and profiles of the Reynolds shear stresses. The most dynamically significant is the in-plane shear stress  $-\overline{uv}$  in which a similar behavior to  $\overline{u^2}$  is seen as distinctive regions trailing the top and bottom rotor blade tips. Clearly visible in figure 4.13 is that the region of positive  $-\overline{uv}$  is always associated with the top of the rotor and dies off slower than the negative region associated with the bottom of the turbine blade.

Comparing again the inflow to the exit row of turbines, we see the maximum value of  $-\overline{uv}$  occurs equally in cases OC2 and BCB. This is the different from the case of  $\overline{v^2}$ , where the maximum intensity of the far wake depended on recovery of the ABL ahead of the nearest upstream turbine. Here, the greatest value of  $-\overline{uv}$  reaches a peak in the *least* recovered wakes.

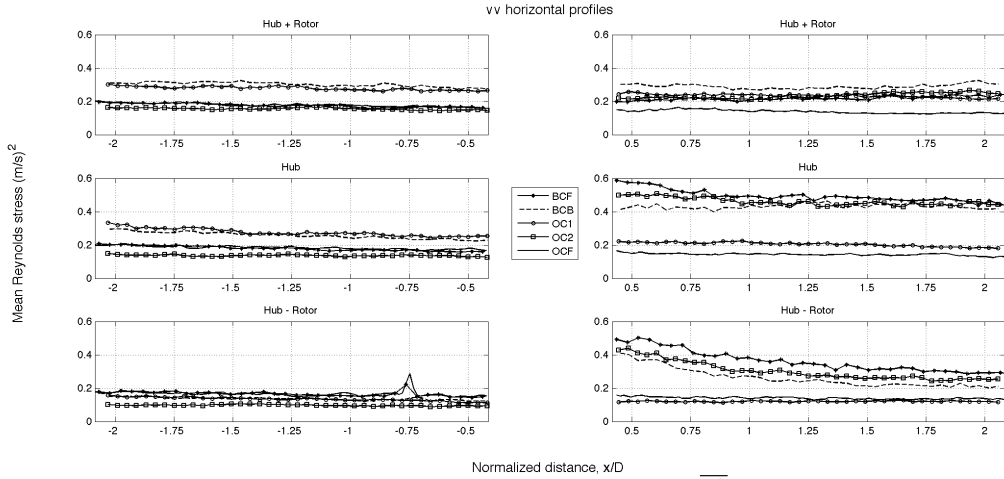


Figure 4.10: Profiles of streamwise normal Reynolds stress,  $\bar{v}^2$  according to the streamwise coordinate. Profiles shown correspond to the hub of the rotor  $\pm$  the radius of the rotor.

## 4.4 Flux of kinetic energy

One of the most important quantities discussed in terms of wake recovery and wind turbines is the flux of kinetic energy,  $F_{ij}$ . Recent studies [11, 23] have shown that the entrainment of kinetic energy vertically downward from outside the rotor canopy is the major factor in transition of the wake toward upstream conditions. In the limit of distance, the wake recovers entirely to the undisturbed ABL. Figure 4.15 shows the flux of kinetic energy comprised from measurements taken. As all measurements were taken in the  $x - y$  plane, measurement sensitivity was low in the spanwise direction. It was also shown that components of  $F_{ij}$  involving  $w'$  or  $W$  were orders of magnitude lower than those including only the streamwise and wall-normal components. In figures 4.15 and 4.16 the only component shown is  $F_{12} = -\bar{u}\bar{v}U$  as it is the dominant contributor to the total.

Note that like in the preceding contour plots, the upstream positions for the entrance rows corresponds to the ABL inflow, free of disturbances. One can observe that in the leftmost subfigures, the magnitude of  $F_{12}$  shows a maximum value of about  $0.4 \text{ m}^2/\text{s}^2$  at  $y/D \approx \frac{1}{2}$ . In all other positions, the maximum occurs in the top area of the rotor. This is a result of the high level of agitation in the flow from the combination of a high mean velocity and the periodic presence of a moving solid boundary.

In the right two columns of subfigures (those corresponding to the exit row turbines),  $F_{12}$  is shown to show a net positive downward trend even in the far wake.

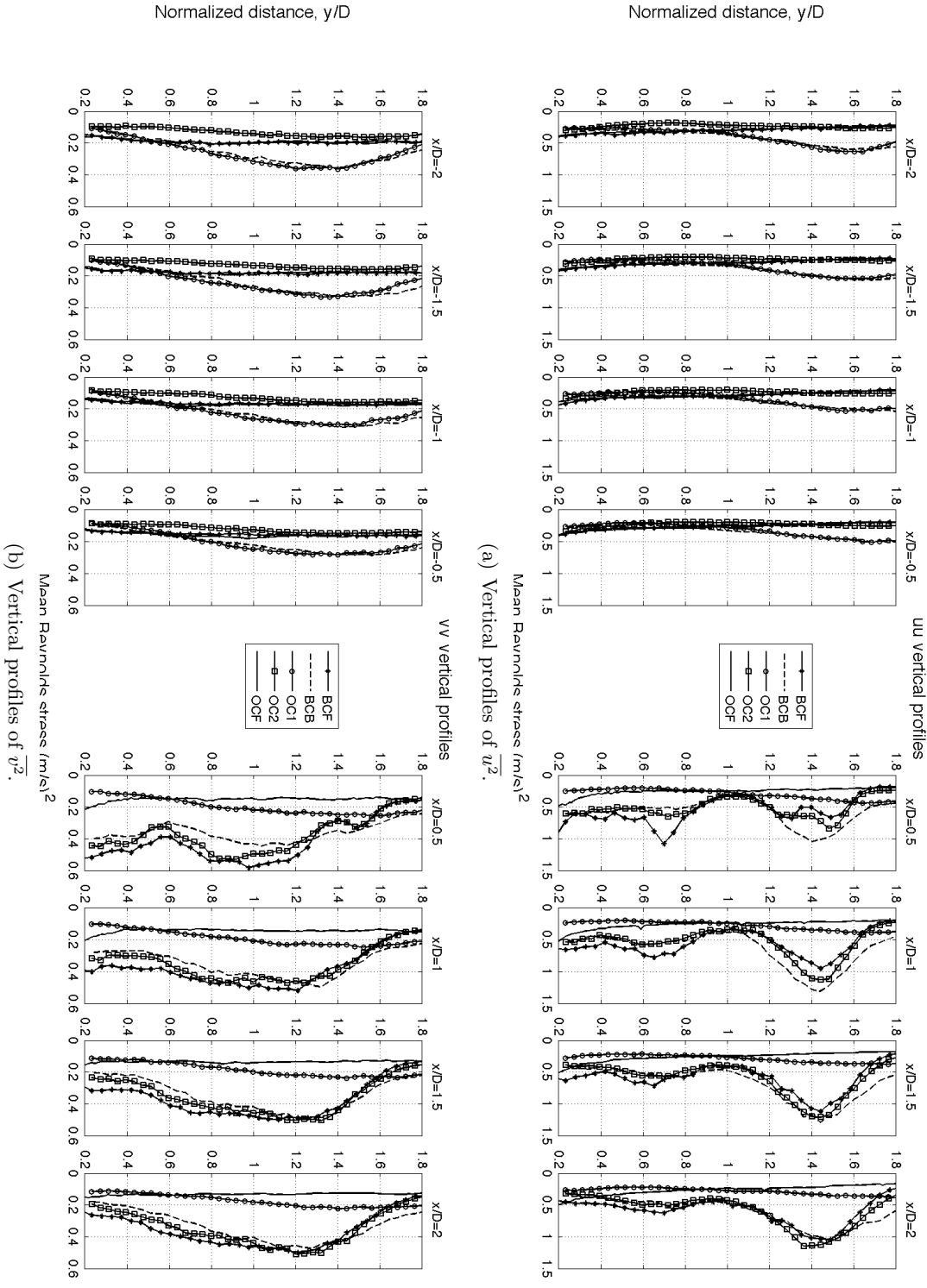


Figure 4.11: Profiles of Reynolds normal stresses in streamwise 4.11(a) and wall-normal 4.11(b) directions according to the wall-normal coordinate. Profiles are taken at half-diameter distances ( $x/D = \pm 0.5 \times n, n \in [1, 2, 3, 4]$ ) upstream and downstream of wind turbine model.

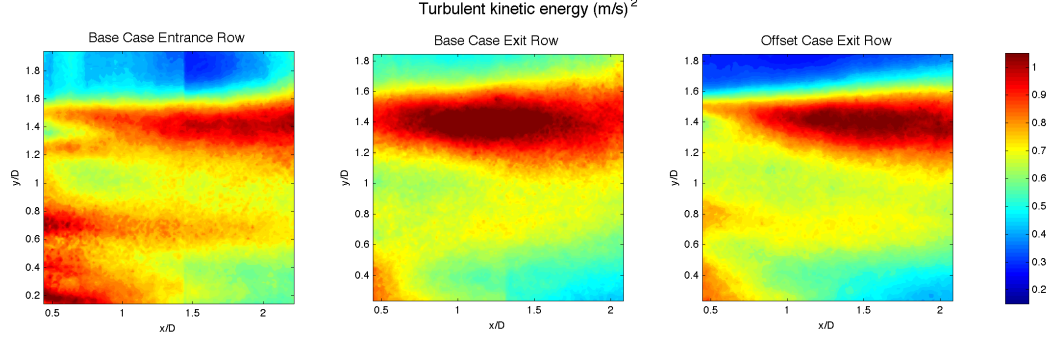


Figure 4.12: Contour plots of turbulent kinetic energy,  $k = \frac{1}{2}(\bar{u}^2 + \bar{v}^2 + \bar{w}^2)$ .

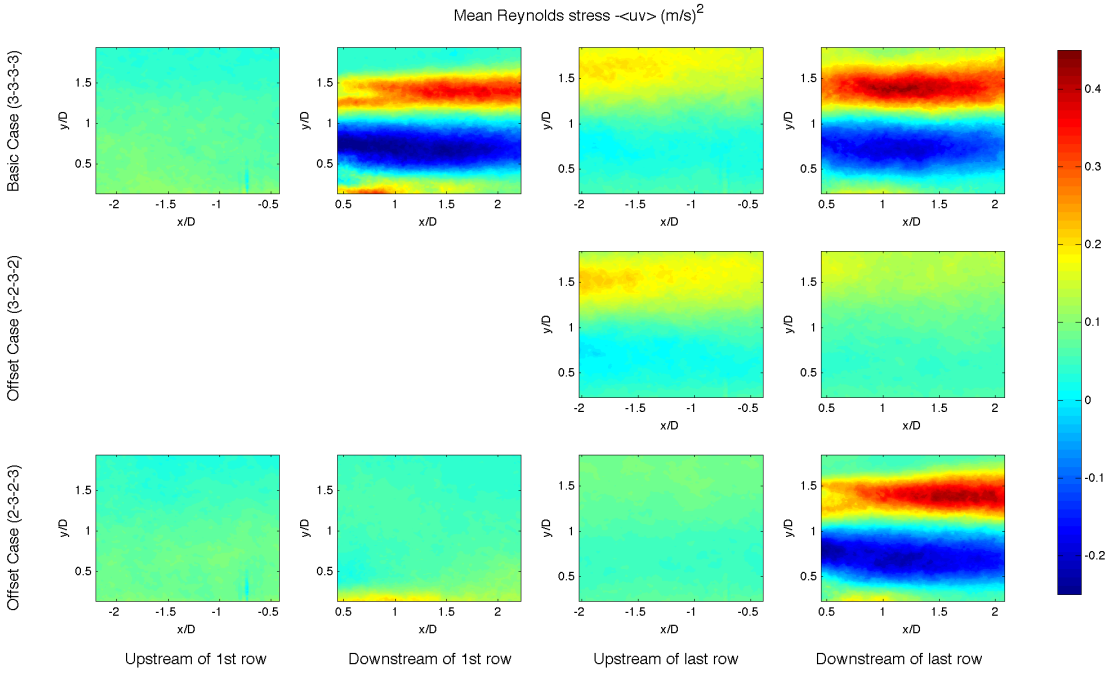


Figure 4.13: Contour plots of  $-\bar{u}\bar{v}$  for all SPIV locations delineated in figure 2.7.

The bottom row of subfigures shows the offset arrangement in which the wake has had 10 to 12 rotor diameters to recover (bottom right pair). In this position  $F_{12}$  is still greater in the top of the canopy. This implies that even 12 rotor diameters downstream of a turbine, the ABL is still not recovered and kinetic energy is still being supplied from above to supplement the momentum deficit in the array.

It can be observed that  $F_{12}$  also seems to be additive with itself, meaning that in the exit row of the base arrangement (top right pair) where the inflow shows high levels of downward entrainment,  $F_{12}$  in the outflow is not as concentrated or localized as in the entrance row of the base arrangement or even the exit row of the offset case, where the wake has dissipated considerably. Figure 4.16 shows only the near wakes of the wind

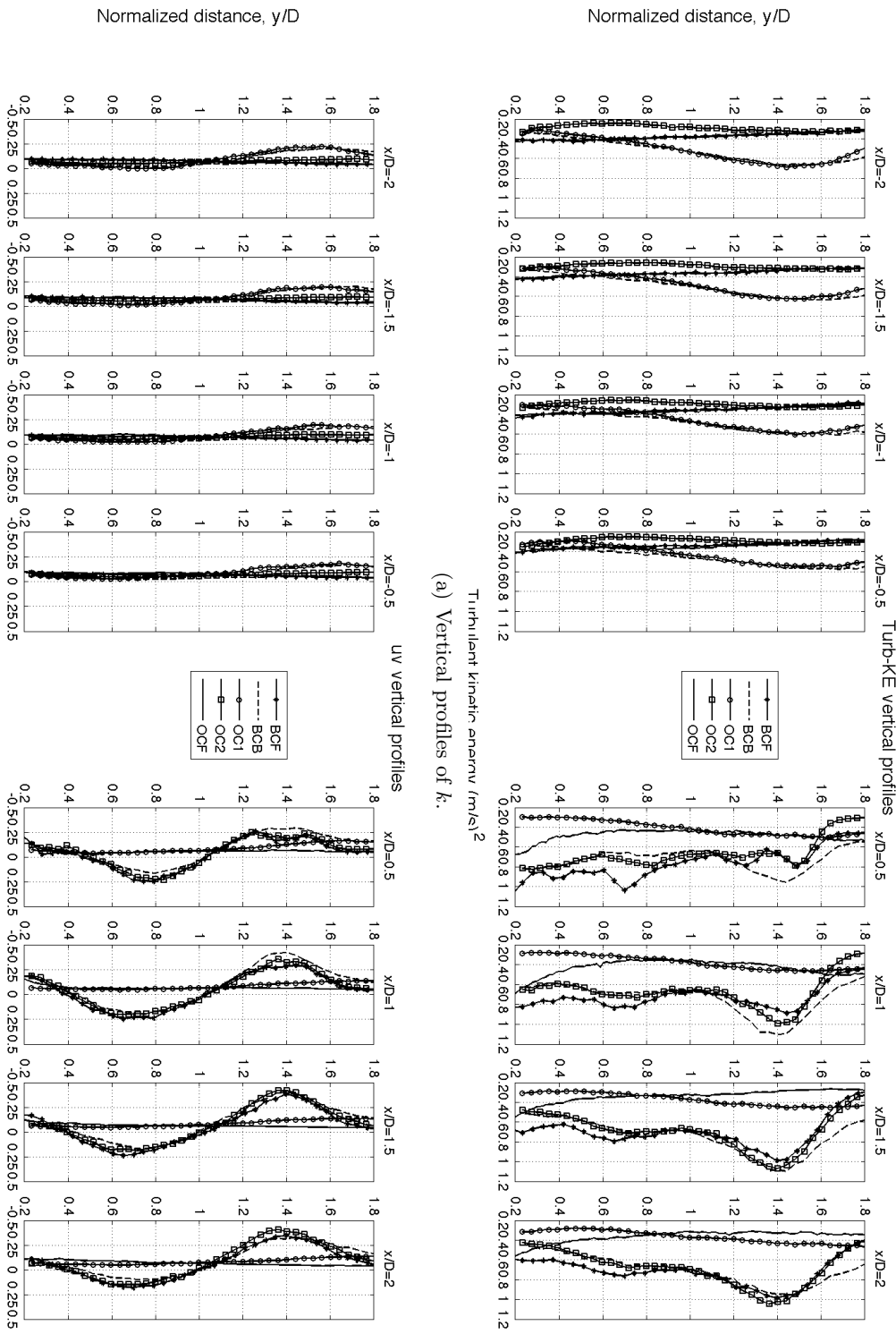


Figure 4.14: Profiles of turbulent kinetic energy (4.14(a)) and the Reynolds stress  $-\bar{u}\bar{v}$  (4.14(b)). Profiles are taken at half-diameter distances ( $x/D = \pm 0.5 \times n$ ,  $n \in [1, 2, 3, 4]$ ) upstream and downstream of wind turbine model.

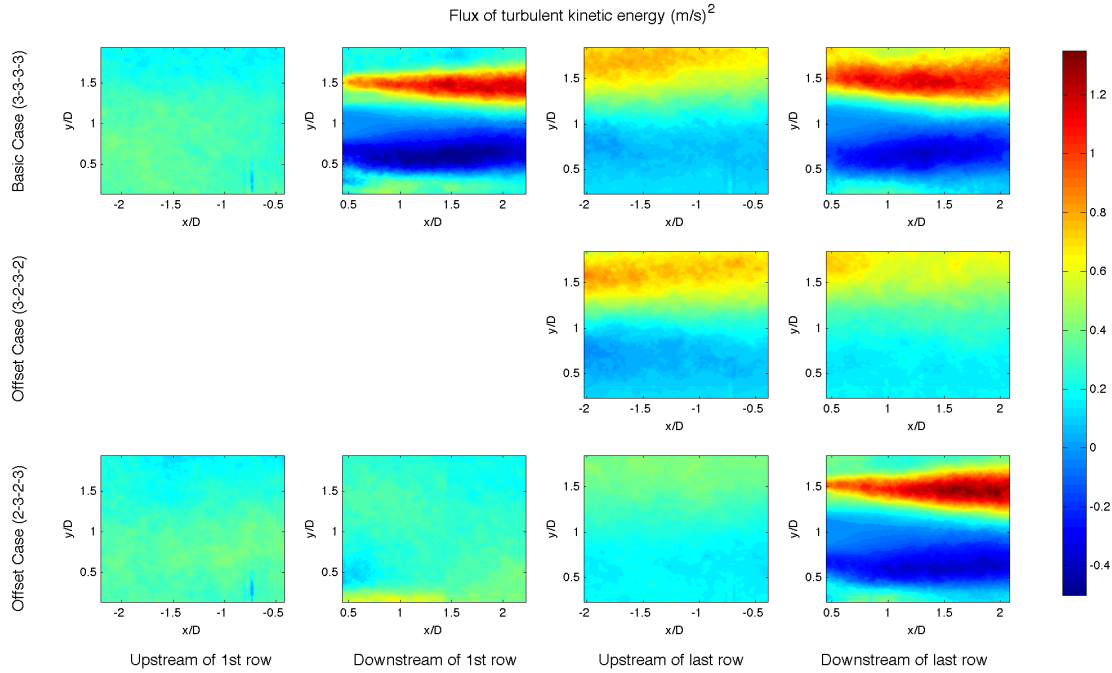


Figure 4.15: Contour plots of flux of kinetic energy,  $F_{ij}$ . As in turbulence production, only the streamwise and wall-normal components are shown as  $F_{12} = -\bar{uv}U$  as dominant contributor to the whole.

turbines for easier comparison. Note that the detail comparison makes clear that the entrance row turbine actually shows the minimum value of  $F_{12}$ , that is flux of energy upward from below the turbine canopy area.

## 4.5 Additional quantities of interest

As illustrated in the introduction, vorticity,  $\Omega$ , is one of the many quantities used to characterize or gauge turbulence. As the vorticity can be directly related the stretching and compression of turbulent structures, it is a good check of general patterns of motion. Figure 4.17 shows the spanwise component of vorticity  $\Omega_z$ . Due to its rotational nature, the spanwise component of vorticity actually acts in the measurement plane shown. According the right-hand rule, a positive value of  $\Omega_z$  is directed vectorially out of the page and corresponds to counter-clockwise motion.

Positive values of vorticity are shown in an ensemble mean sense to exist only in the bottom area of the rotor. This rotation is akin to stating that the ejections of low energy fluid from the near-wall zone is increased in the bottom area of the rotor. Conversely, the top area of the measurement planes show a negative mean value of  $\Omega_z$ .

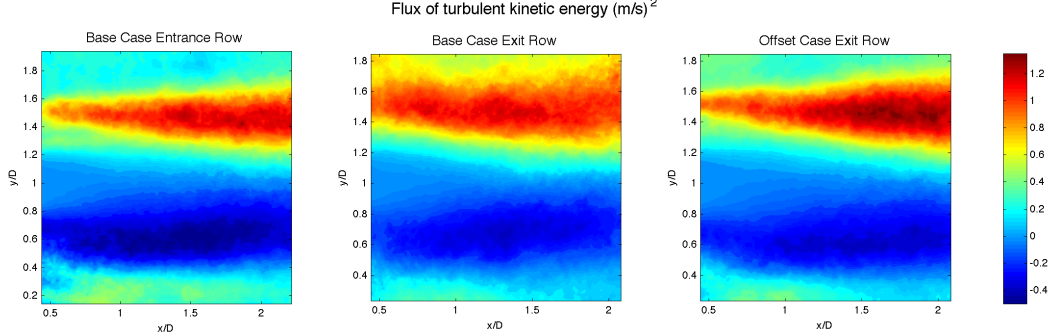


Figure 4.16: Comparison of flux of kinetic energy  $F_{12}$  for wake areas only. Wakes correspond to BCF, BCB, and OC2 from left to right.

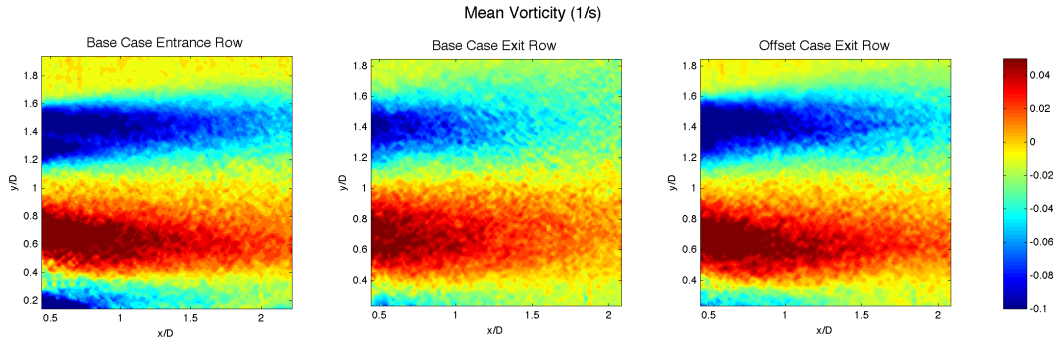


Figure 4.17: Contour plots of spanwise component of vorticity,  $\Omega_z = \frac{\partial U}{\partial y} - \frac{\partial V}{\partial x}$  for all SPIV locations delineated in figure 2.7.

This corresponds in the same way to motion downward of high velocity fluid from above the turbine canopy. Similar results were discussed in [23].

The measurement locations omitted from figure 4.17 include the inflow to the turbines and locations in which there was no wind turbine model. In all omitted measurement locations, the vorticity was of low orders of magnitude and do not illustrate well the wake dynamics in question. It is interesting to note in figure 4.17 that the magnitude of the vorticity in all three of the wakes is very similar below the turbine canopy. The only substantial difference between the three being a negative region due to recirculation around the mounting plate in the entrance row (leftmost subplot). The exit row of the base configuration (the middle subplot) shows slightly reduced magnitudes of  $\Omega_z$ , on the order of 5 – 10% less than the other wakes.

As mentioned in Chapter 1, the production of turbulence is a quantity that can be used to assess the rate at which energy is removed from the pool available to wind turbines in the array. The contours presented in figure 4.18 show clearly that the structures associated with the top and bottom tips of the rotor area are those responsible

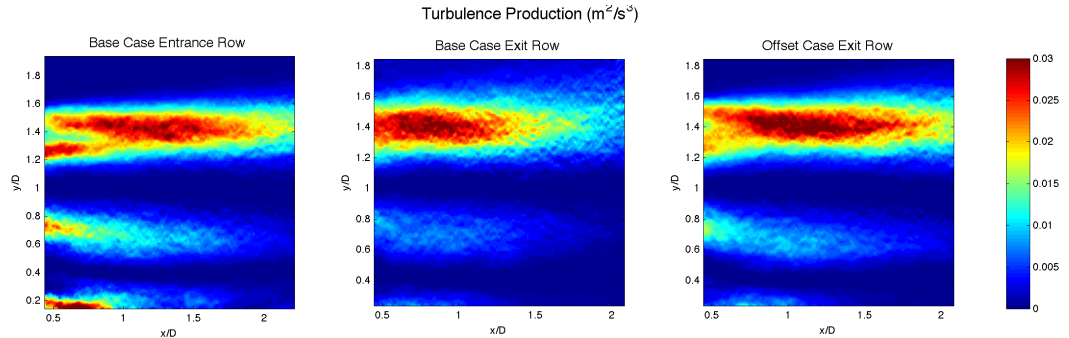


Figure 4.18: Contour plots of turbulence production. Here, the only component of  $\mathcal{P}_{ij}$  shown in  $\mathcal{P}_{12} = -\bar{uv}\frac{\partial U}{\partial y}$ . The contribution of  $\mathcal{P}_{12}$  to the total turbulence production was between 1 and 4 orders of magnitude greater than other components.

for the greatest production of  $k$ . This also means that the greatest portion of mean energy to turbulent energy is converted by the tip vortices of the rotor. Structures arising from the presence of the nacelle and mast in the mean flow contribute orders of magnitude less to the production of turbulence.

Figure 4.18 highlights the contributions to the production of turbulence by tip-vortices in the entrance row of the base arrangement (leftmost subfigure) and the exit row of the offset arrangement (rightmost subfigure). The region of the greatest magnitude of production is also very well defined in every case and position. This demonstrates that the “productive” region of the wake, in the sense of turbulence, is localized to the near-wake region. This is in direct contrast to quantities such as the flux of kinetic energy as seen in figure 4.15, where activity can be seen clearly up to 10 rotor diameters downstream.



# Chapter 5

## Results of Snapshot POD

### 5.1 Validation of POD methods

A POD analysis code was developed to formulate the empirical correlation tensor denoted by equation 1.38. The code was then run for the data collected in the experiment delineated in Chapter 3 according to several schemes. The kernel of the POD was varied to test the rate of accumulation of energy in the eigenvalue based on inclusion of the out-of-plane velocity component,  $w$ . Table 5.1 shows the four POD schemes tested in the present analysis and the number of modes required to amass 50% of the energy for each case, both in upstream and downstream positions relative to the wind turbine model.

Table 5.1: Total energy,  $E = \sum \lambda_n$ , in the upstream and downstream positions of BCB according to POD method.

		$\sum \lambda$	Modes for 50% energy
3-component, instantaneous data	upstream	1.8674e+04	73
	downstream	1.1812e+05	306
2-component, instantaneous data	upstream	8.8552e+03	18
	downstream	2.7680e+04	201
3-component, fluctuating data	upstream	1.9846e+04	56
	downstream	1.1958e+05	299
2-component, fluctuating data	upstream	1.0026e+04	13
	downstream	2.9156e+04	168

Due to the tendency of the POD to organize motions and structures within the flow according to energy content, the first mode of the POD when *instantaneous* data is used as the kernel contained almost exclusively mean flow statistics,  $\mathbf{U}$ . Thus, when looking at the energy contained in *turbulent* structures, the accumulation of energy begins at

with the second mode as  $E_{inst} = \sum_{n=2}^{2000} \lambda$ . The reconstruction of velocity fields based on the first mode was not exactly identical to the mean flow. As the POD organizes structures according to energetic motion, there was some exchange of information where the value of the mean flow statistics and fluctuations of velocity were at the same order of magnitude. Figures 5.1 and 5.2 highlight the areas in which the exchange of information described above is most visible. The regions within the data fields showing the greatest error were those most susceptible to numerical error, that is where mean velocity is near zero.

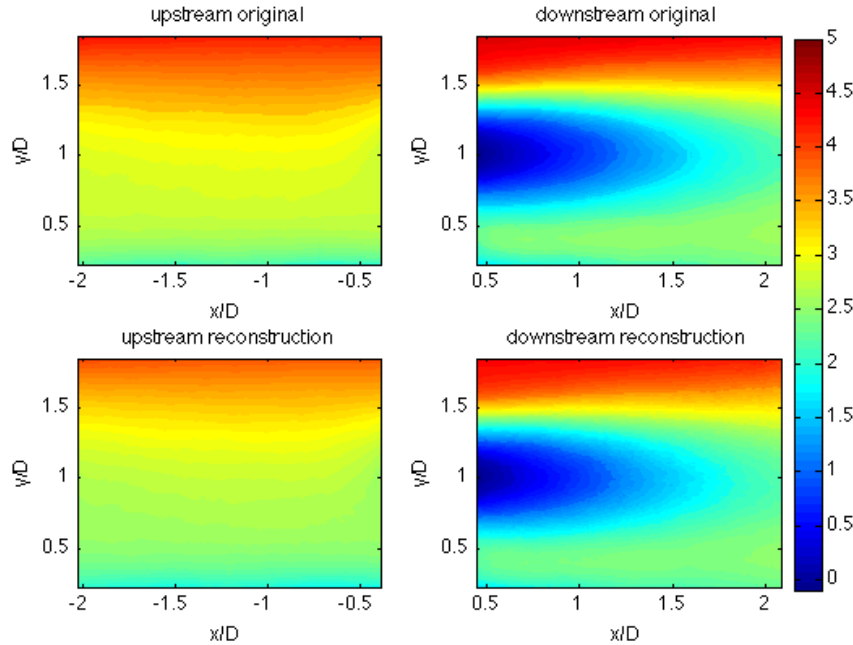


Figure 5.1: Comparisons of original statistical data and reconstructed mean using only the first mode of POD with instantaneous data for upstream and downstream positions.

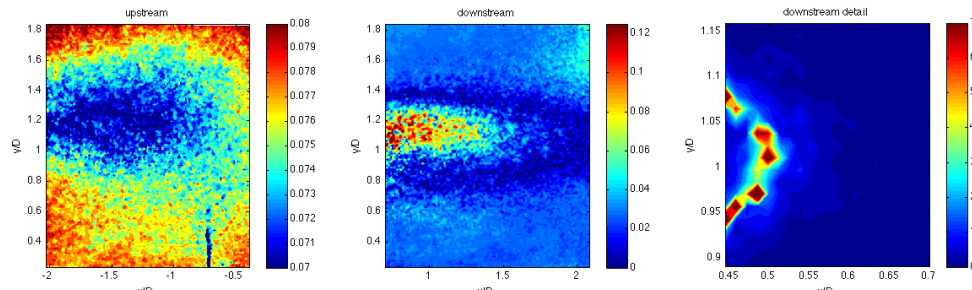


Figure 5.2: Relative error between the velocity fields compared in figure 5.1. Error is defined as  $Err_{rel} = |U - U_{rec,n=1}|/U$ . The downstream position (right) is a detail section of the rotor hub area where numerical error is most significant. In the upstream window, error is bound from approximately 0 – 3%. In the downstream area, the error can be *very* large due to division by near zero elements in the near wake.

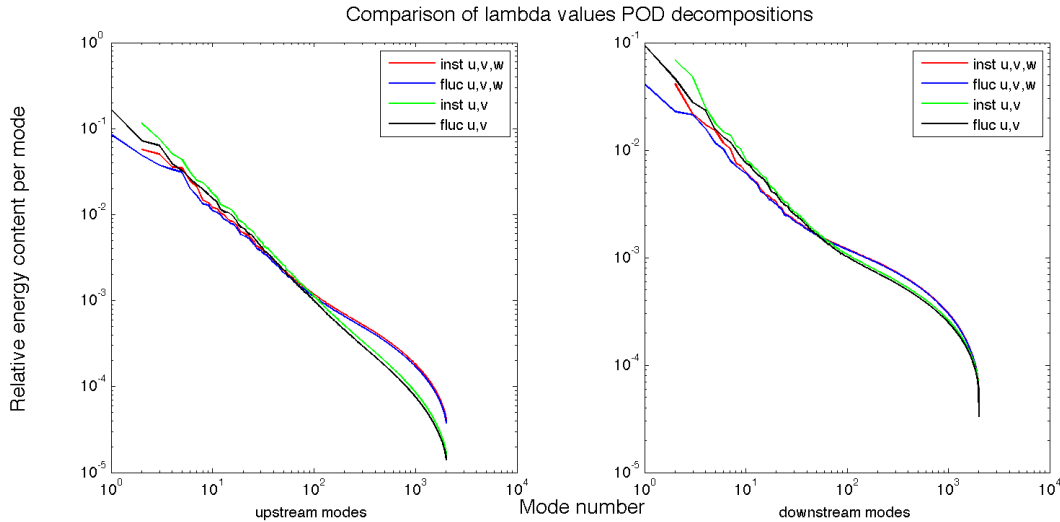


Figure 5.3: Comparison of  $\lambda$  values based on POD method. Note that the instantaneous data starts at mode 2 (the first mode is the mean flow) and that including the  $w$  component increases the relative energy content at smaller modes. Solid lines correspond to upstream positions, dashed lines correspond to downstream positions.

Figure 5.3 compares the accumulation of energy in  $\lambda$  according to the POD schemes described above. The kernels that include the spanwise component of velocity (red and green) show a small vertical offset of energy according to POD mode. This offset is related to the contribution of the turbulent kinetic energy by the  $\overline{w'^2}$ . The POD built with the instantaneous flow kernel shows less energy in the eigenvalues associated with lower modes (larger structures) and more energy at higher modes (smaller structures) than the eigenvalues built including only fluctuating data.

The most significant difference demonstrated in figure 5.3 is that the inclusion of  $w$  leads to a significant accumulation of energy in the smaller structures regardless of whether the kernel contains instantaneous data or the zero-centered fluctuations. This suggests that the energetic turbulent structures measured in the wind turbine wakes in the experiment were largely independent of the spanwise component of velocity,  $w$ . It also suggests that many phenomena associated with small scales of turbulence, such as the dissipation of energy into heat, are sensitive to spanwise velocity fluctuations within a turbine array.

A further comparison of the POD based on the four kernels suggested above is shown in figure 5.4. The exchange of information between mean and fluctuating velocities discussed above is evident in the four reconstructions. Using the instantaneous data in the POD kernel results in leakage of energy from the Reynolds stresses to the mean

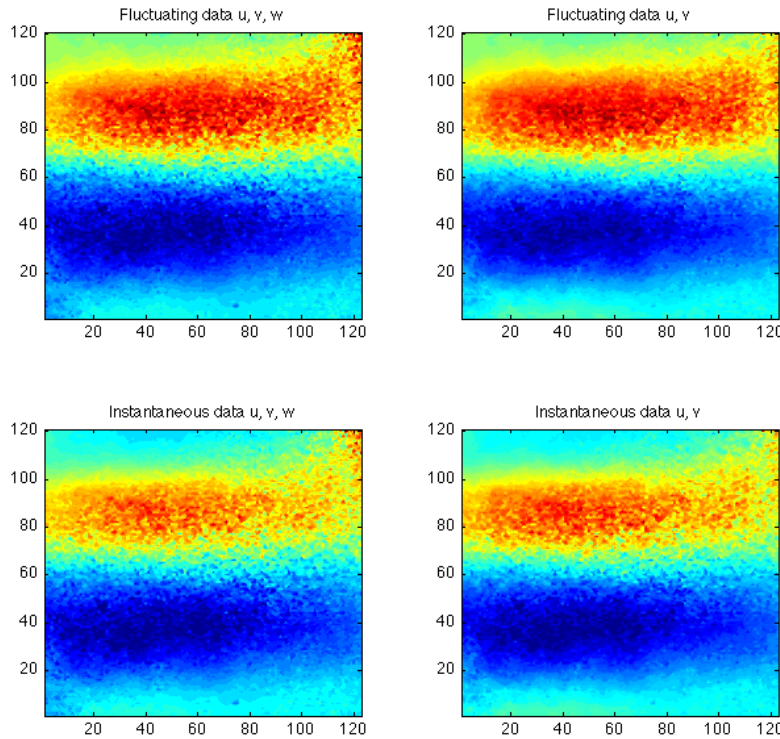


Figure 5.4: Comparison of the reconstructed Reynolds stress  $-\bar{uv}$  according to four different POD schemes. From top left, clockwise, three component POD of fluctuating data, two component POD of fluctuating data, two component POD of instantaneous data, three component POD of instantaneous data. In each case, only modes required to rebuild 50% of the total energy were used. Reconstructed velocities correspond to the near-wake area of the exit row turbine in the base arrangement.

velocity. Additionally it is suspected that there is some leakage of energy from  $u$  and  $v$  into the spanwise component  $w'$ . The reconstruction of  $-\bar{uv}$  using two-component fluctuating data not only requires fewer modes than the other kernels, it also most closely resembles the original statistics shown in figure 4.13. For this reason, the results presented in §5.2 are all based on the kernel of the POD formed with two-component, fluctuating data. With this kernel, the reconstruction rate is optimized as seen in the accumulation of energy by eigenvalue. Table 5.2 shows the number of modes required to rebuild several selected levels of the turbulent energy.

Table 5.2: Modes required to reconstruct a prescribed portion of turbulence energy (upstream–downstream)

	BCF	BCB	OCF	OC1	OC2
Modes for 50% energy	30 – 348	13 – 168	38 – 39	13 – 10	8 – 42
Modes for 75% energy	266 – 860	94 – 661	317 – 324	85 – 77	61 – 349
Modes for 90% energy	789 – 1370	488 – 1222	857 – 845	404 – 410	323 – 918
Modes for 95% energy	1158 – 1621	883 – 1561	1219 – 1204	758 – 776	640 – 1282

## 5.2 POD results

Table 5.2 clearly states that the upstream position of each measurement location rebuilds with fewer modes than the downstream position with the exception of the exit row position in the (3-2-3-2) offset arrangement. This agrees well with expected results as the turbulence coming into a turbine position is less than that of the outflow.

To rebuild 50% of the energy in the inflow, between 0.4% and 1.9% of the modes are required. For the outflow up to 17.4% of the modes are required to reach the 50% threshold. For OC1, an exit row position where there is no turbine, the modes required to rebuild a given percentage of the energy are *more* in the upstream position. Again, this agrees with expectations as the turbulence in the wake is dying out as the mean ABL recovers to its upstream conditions. The decay (and dissipation) of turbulence is from the small scales resulting in an apparent accumulation of energy content of the large scales. The inflow of OC2, an exit row position *with* a turbine, has had between 10 and 12 rotor diameters to recover. This is also the position requiring the fewest modes to reconstruct a 50% of turbulent energy, approximately 20 – 30% of the modes required to reach the same energy level for inflow to the turbine array.

Figures 5.5 and 5.6 compare the eigenvalue distributions of all measurement locations using the two-component fluctuating POD kernel. In the two figures, the eigenvalues are normalized to the position of maximum turbulent energy and to themselves, respectively. In figure 5.6 a line is included to show the common fall-off of eigenvalues according to the power relationship  $n^{-1.17}$ .

It is well known that when the input data for the POD is homogenous, the resulting POD modes are identical to Fourier modes. Thus in positions where there is at least a *weak* homogeneity, the POD modes demonstrate some Fourier-type behavior. This is evident often in the upstream windows of many of the measurement locations. In such positions, the gradients in the streamwise direction is very small compared to the wall-normal direction. Thus the POD modes shown in figure 5.7 demonstrate some

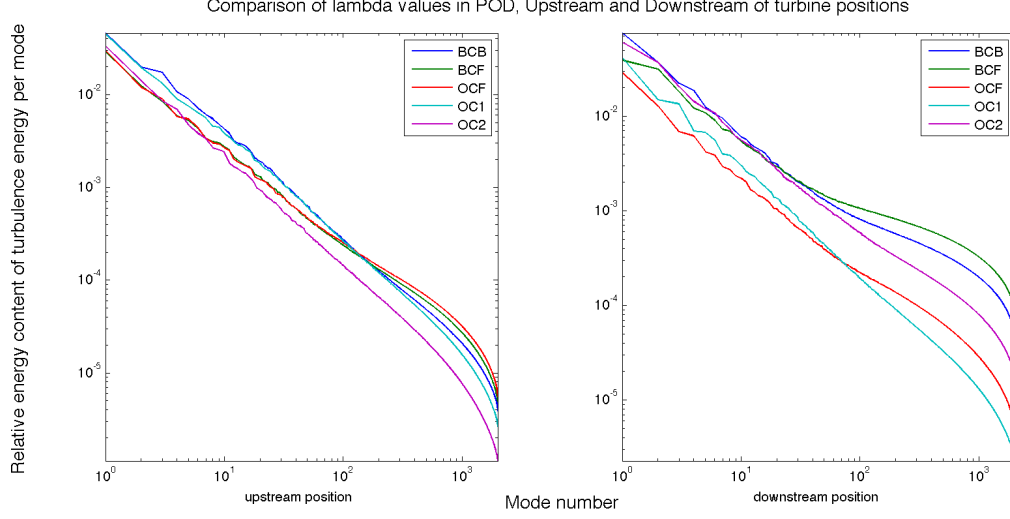


Figure 5.5: Comparison of  $\lambda$  values for each measurement position. The subplot on the left is the upstream location for each case and the right is downstream. Note that the first mode for all cases is higher downstream than upstream. Here, all eigenvalues were normalized by the maximum sum, the sum of eigenvalues corresponding to the downstream window of BCF.

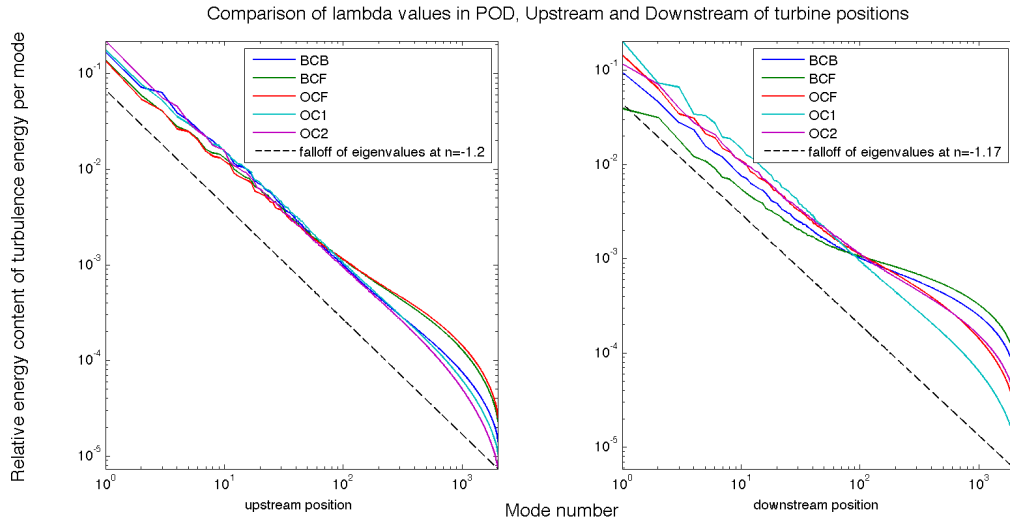


Figure 5.6: Comparison of  $\lambda$  values for each measurement position. The subplot on the left is the upstream location for each case and the right is downstream. Note that the first mode for all cases is higher downstream than upstream. Here, all eigenvalues were normalized by themselves. That is  $\sum \lambda_n = 1$ . The black dot-dashed line describes the fall-off of  $\lambda$  values as  $n^{-1.17}$ .

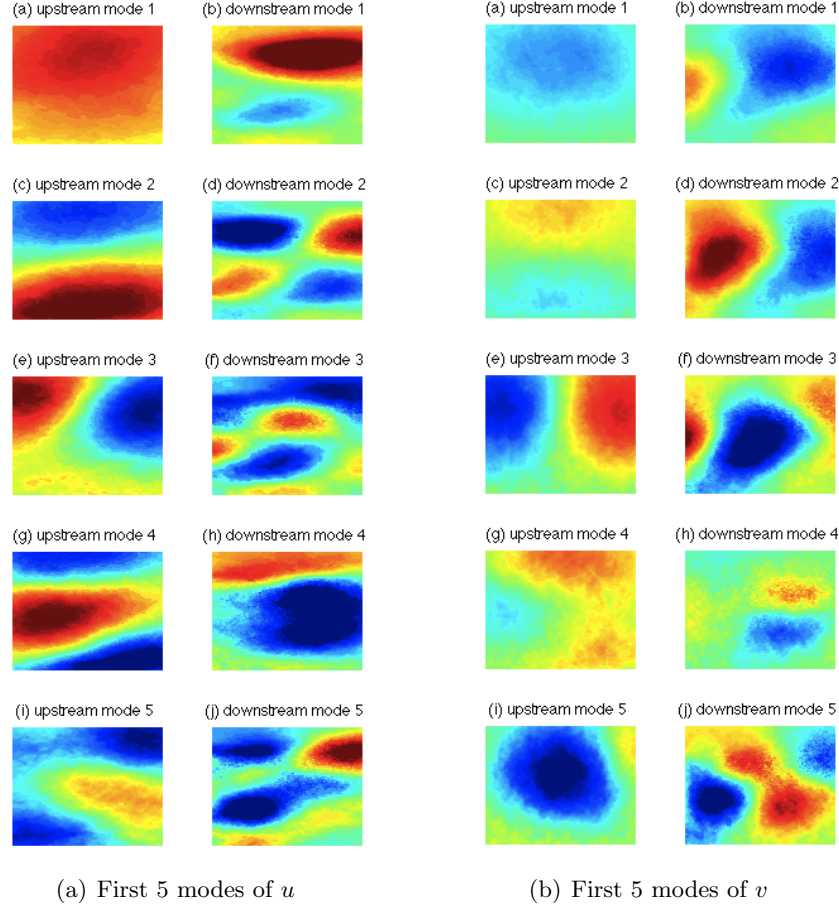
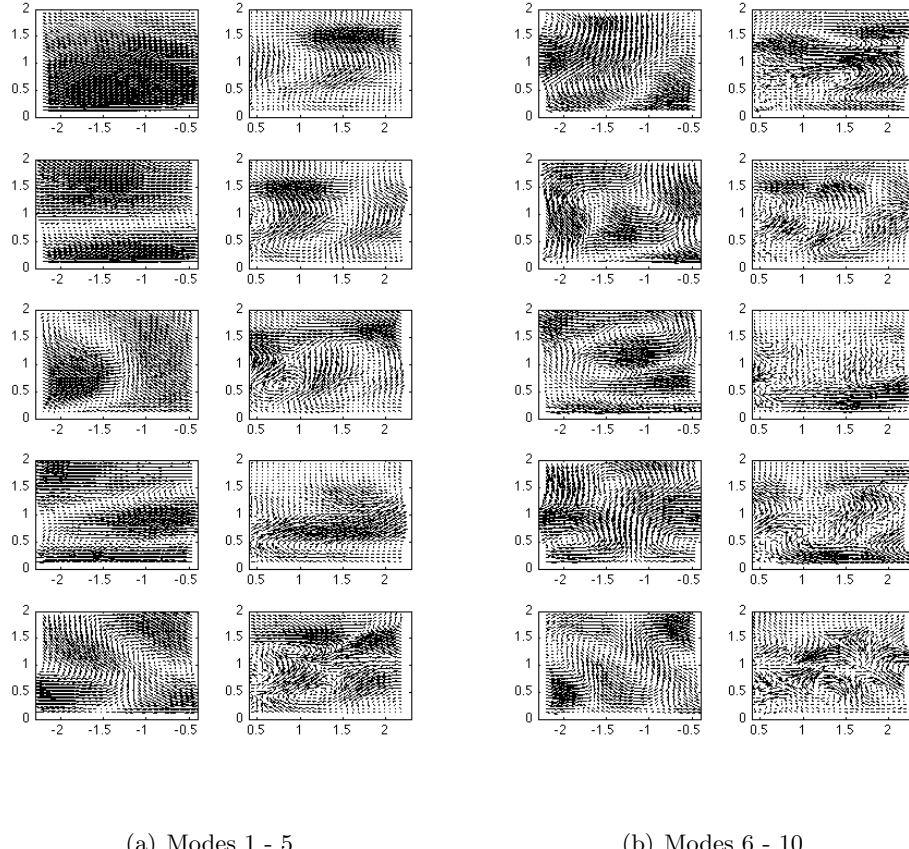


Figure 5.7: Contour plots for the first 5 modes resulting from the snapshot POD, in subfigure 5.7(a),  $\Phi_u^n$  and in subfigure 5.7(b),  $\Phi_v^n$  where  $n \in \{1, \dots, 5\}$ . From top to bottom are modes 1 through 5, respectively. From left to right

wave-like Fourier behavior in the streamwise direction.

The POD executed in this research used *vectorial* flow measurements to build the correlation kernel. The POD modes,  $\Phi_u$  and  $\Phi_v$ , shown in figure 5.7 can be combined in a vector sense as in figure 5.8. The modes  $\Phi_u$  and  $\Phi_v$  are orthogonal in a *physical* sense whereas subsequent modes of the POD are orthogonal in the sense of linear algebra.

The POD modes shown in figures 5.7 and 5.8 are simply demonstrative of the orthogonal vector basis produced by the POD. The magnitudes of the modes have no physical relevance on their own. It is only when the modes are multiplied with their respective random coefficients,  $a_n$ , according to equation 1.40 that the modes are representative of physical phenomena. Figure 5.9 shows some the mean flow statistics reconstructed with both the POD modes and the random coefficients.



(a) Modes 1 - 5

(b) Modes 6 - 10

Figure 5.8: Vectorial POD modes composed of both  $\Phi_u$  and  $\Phi_v$ . In each subfigure, the modes increase going downward. The ordinate is normalized wall-normal coordinate,  $y/D$ , and the abscissa is the normalized streamwise coordinate  $x/D$ . Note the increasing structural complexity moving from mode 1 to mode 10.

Comparing the Reynolds stresses in the figure to those presented in Chapter 3 one can see that relatively few modes are required to achieve intensities on the same order as the original data. After only 5 modes, all three stresses shown ( $\bar{u^2}$ ,  $-\bar{uv}$ , and  $\bar{v^2}$ ) already show the structure seen in mean stress statistics. The same ranges of intensities were used in figure 5.9 as in figures 4.7, 4.8, and 4.13. Note that the energy contained in stresses  $\bar{u^2}$  and  $-\bar{uv}$  reconstructs very quickly whereas  $\bar{v^2}$  requires many more modes to match the original statistical values.

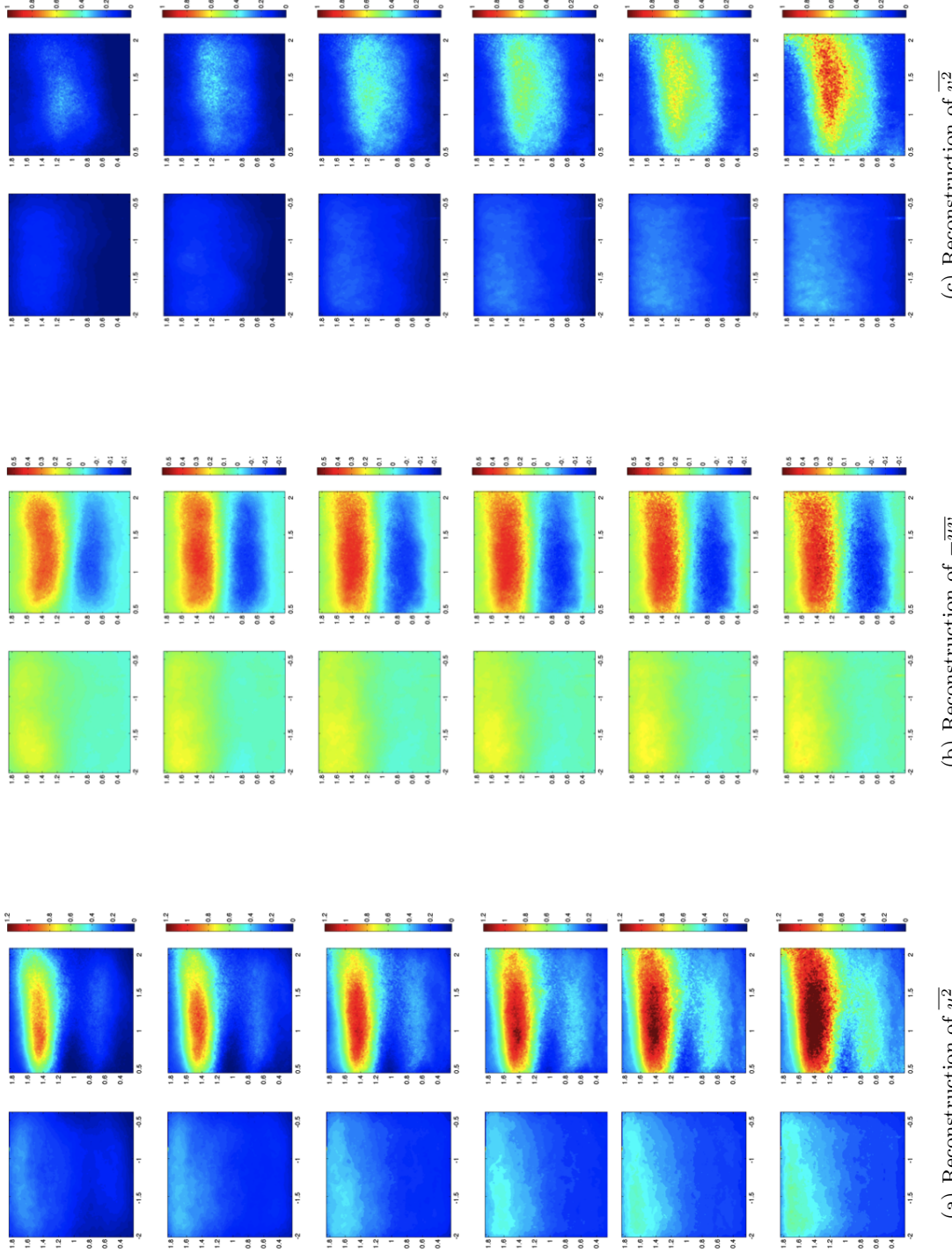


Figure 5.9: Reconstruction of mean Reynolds stresses  $\bar{u}^2$  5.9(a),  $-\bar{uv}$  5.9(b), and  $\bar{v}^2$  5.9(c). Velocity reconstructions are composed of POD modes  $\Phi_u^n$  and  $\Phi_v^n$  shown in figure 5.7 according to equation 5.7. The number of modes used in the reconstructions by row from top are, 5, 10, 25, 50, 100, and 200.

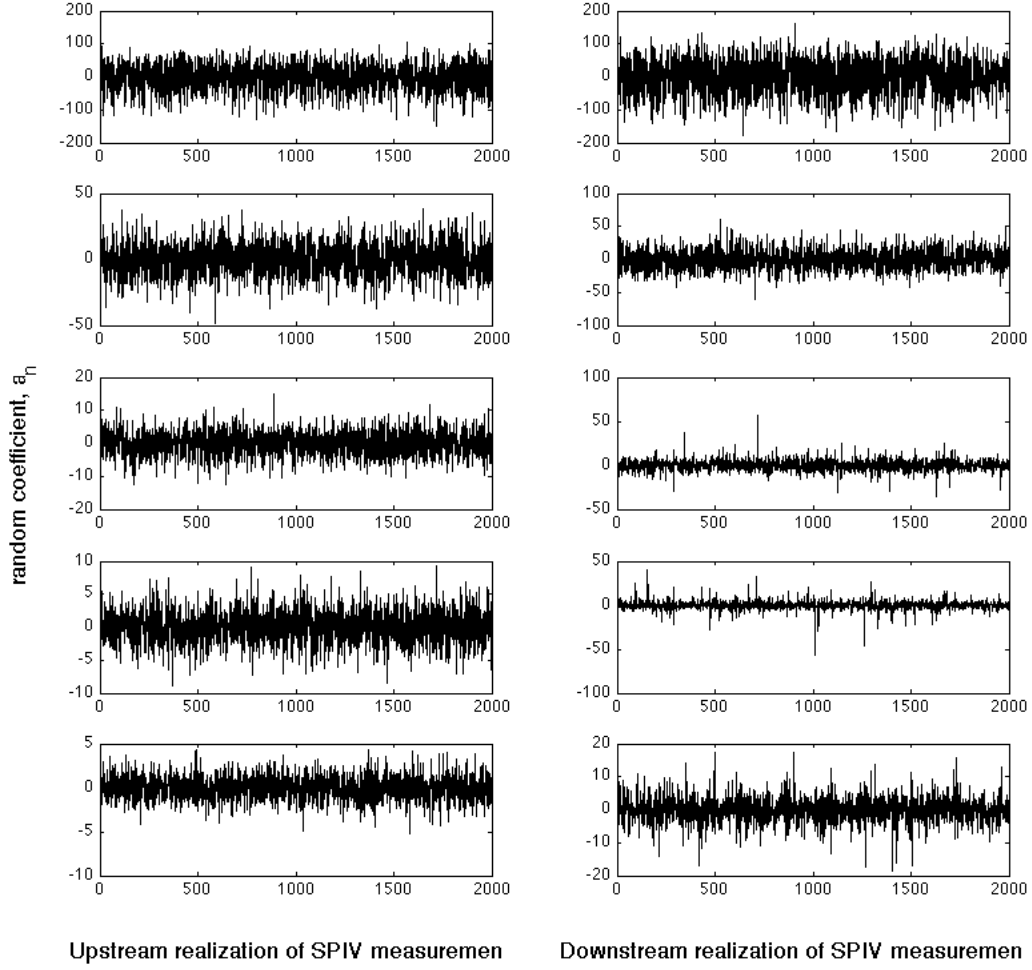


Figure 5.10: Random coefficient,  $a_n$  of the POD. Here shown are the random coefficients corresponding to a single POD mode,  $\Phi_u$  or  $\Phi_v$ , where the abscissa is the indexed number of SPIV measurements.

To demonstrate the random nature of the coefficients  $a_n$ , figure 5.10 shows the magnitudes of the coefficients as a function of the realization of SPIV measurement. Here the POD mode number was held constant for each subfigure. These are the coefficients multiplied by  $\Phi_u$  and  $\Phi_v$  to recover the fluctuating fields of  $u$  and  $v$ , respectively. The coefficients shown in figure 5.10 are indeed randomly distributed and centered about zero.

However, when looking at figure 5.11 one observes a very different behavior. In the figure the random coefficients are organized according to specific realizations of SPIV measurements and the abscissa shows the POD mode number. Here the trends of  $a_n$

are very distinct. They ubiquitously show greater magnitudes at smaller mode numbers than at high ones. This is demonstrative of the reliance of each reconstruction on the energetic structures. In certain fields, the intermediate modes have a greater relative importance than others. The downstream measurement window (right column) shows this behavior more distinctly than the upstream measurement window, implying that the near-wake area of the turbine has more energy in the intermediate structures than the inflow. This agrees well with theory and expected results.

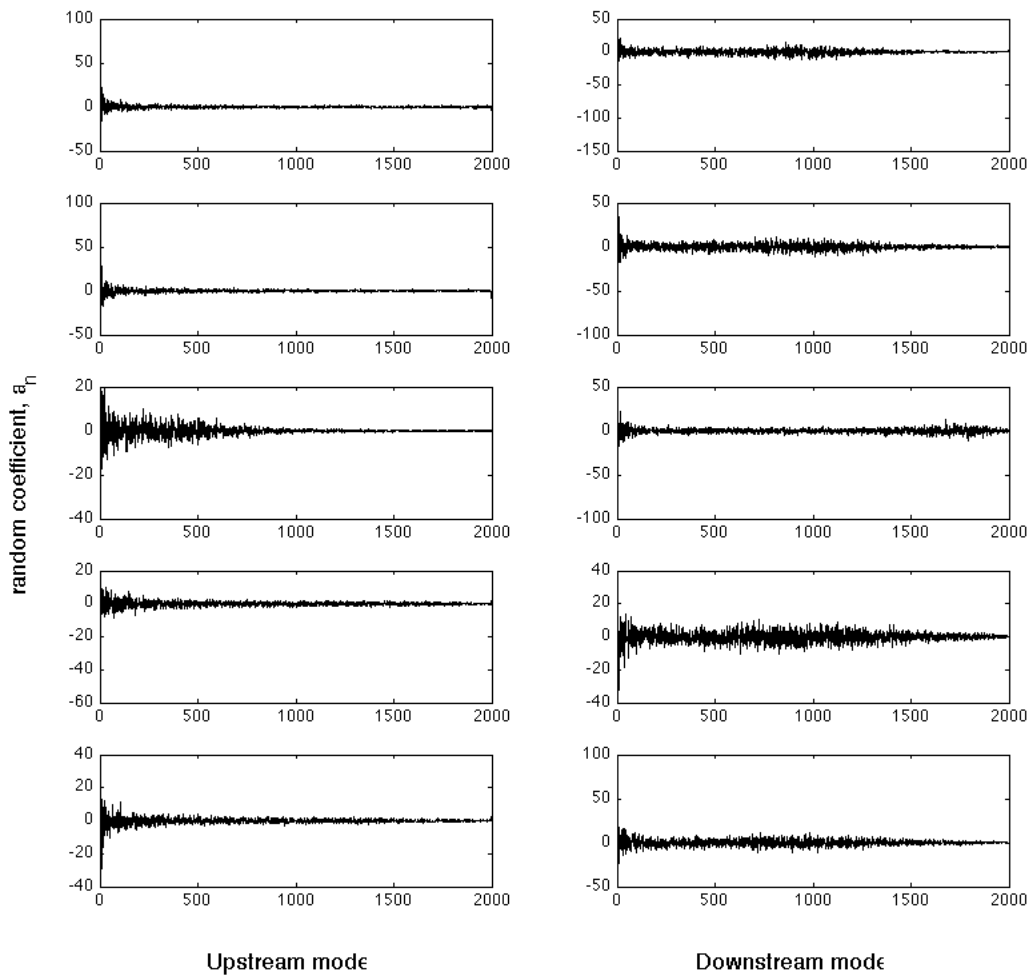


Figure 5.11: Random coefficient,  $a_n$  of the POD. Here shown are the random coefficients corresponding to a single SPIV measurements POD according to mode,  $\Phi_u$  or  $\Phi_v$ . The decay of  $a_n$  with mode number demonstrates that the higher modes contribute less to instantaneous velocity field reconstructions than lower modes. Note that certain fields shower higher values of  $a_n$  at intermediate modes than others.

The normalized mean distribution of  $a_n$  exemplifies this behavior as shown in figure

5.12. Here the random coefficients have been normalized as,

$$a_{n,norm} = \frac{\overline{|a_n|}}{\sum_n^{2000} |a_n|} \quad (5.1)$$

where the overline implies that the mean average was taken across all SPIV windows. Figure 5.13 compares the distribution of the eigenvalues to the normalize mean of random coefficients according to equation 5.1. In the figure, the trend lines corresponding to the downstream measurement window for both  $a_{n,norm}$  and  $\lambda$  show greater magnitudes in the intermediate mode range than in the upstream measurement locations. This comparison is to highlight the trend that both the random coefficients and the eigenvalues are similar in form. The magnitudes of the two trends cannot be directly compared.

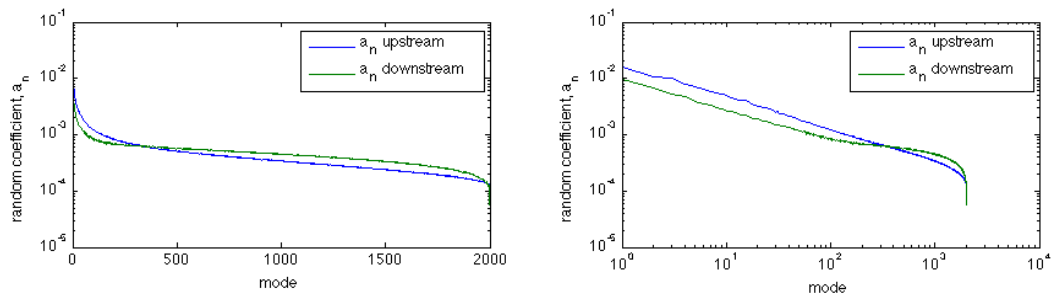


Figure 5.12: Normalized mean distribution of random coefficients according to equation 5.1. The left figure shows the distributions of upstream and downstream normalized mean random coefficients in semi-log scaling and the right figure in logscale. Note the trends of the normalized mean distributions are similar in form to the distributions of the eigenvalues,  $\lambda$ . Figure 5.13 compares the two trends.

A major goal of performing the snapshot POD analysis on the data here was to determine which structures are most significant in the performance of the wind turbine models. The flux of kinetic energy,  $F_{12}$ , discussed in §4.4 is especially important in the recovery of the ABL. The downward entrainment of kinetic energy is responsible for the disappearance of the wake downstream.

Figures 5.14 and 5.15 show the reconstructions of  $F_{12}$  using only 50% of the energy in the flow. In the figures, the reconstructed flux of kinetic energy is nearly identical to the calculations shown in the previous Chapter. This is demonstrative that the vertical entrainment of kinetic energy is reliant on only the large structures of turbulence. Because turbulence is a three dimensional phenomenon and it tends to greatly increasing mixing rates and transport, an *increase* of turbulence kinetic energy in the near wake can

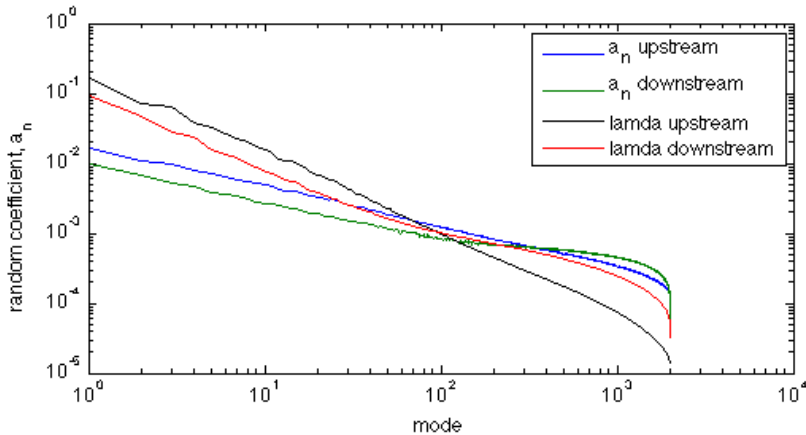


Figure 5.13: Comparison overlay of the normalized mean random coefficients  $a_{n,norm}$  and the eigenvalues  $\lambda$ . Although the fall-off of the two are different, they show similar forms both upstream where the fall-off is very consistent and in the downstream position where the intermediate modes have a more significant contribution.

lead to a shorter recovery length of the wake. The increased energy of large structures in the upper wake area tends to increase the energy entrained from above into the turbine canopy.

By changing the arrangement of the wind turbine array, the specific inflow conditions to each turbine model were in turn affected. The changes exacted in the study here require that the row density of turbines in the array is the same, that is the spanwise spacing of turbines is unchanged from case to case. Staggering the rows such that turbines from row to row are not aligned in the streamwise direction leads to longer recovery periods before subsequent turbines are added. Thus, the streamwise spacing is doubled to 12 times the diameter in the row offset arrangement.

The power curves shown in figure 3.2 and the curves of  $c_p$  shown in figure 3.3 demonstrate that the exit row turbine in the offset case generates more than three times as much energy as that of the base case. It has already been observed that the lower POD modes demonstrate a concentration of relative energy content compared to the full span of modes when moving downstream within the array. This implies that the performance of turbines in different arrangements can be assessed or approximated by the eigenvalues resulting from the POD discussed here. Figure 5.16 shows a ratio of energy contained in modes upstream and downstream of the wind turbines.

$$\kappa = \frac{\lambda_{upstream}}{\lambda_{downstream}} \quad (5.2)$$

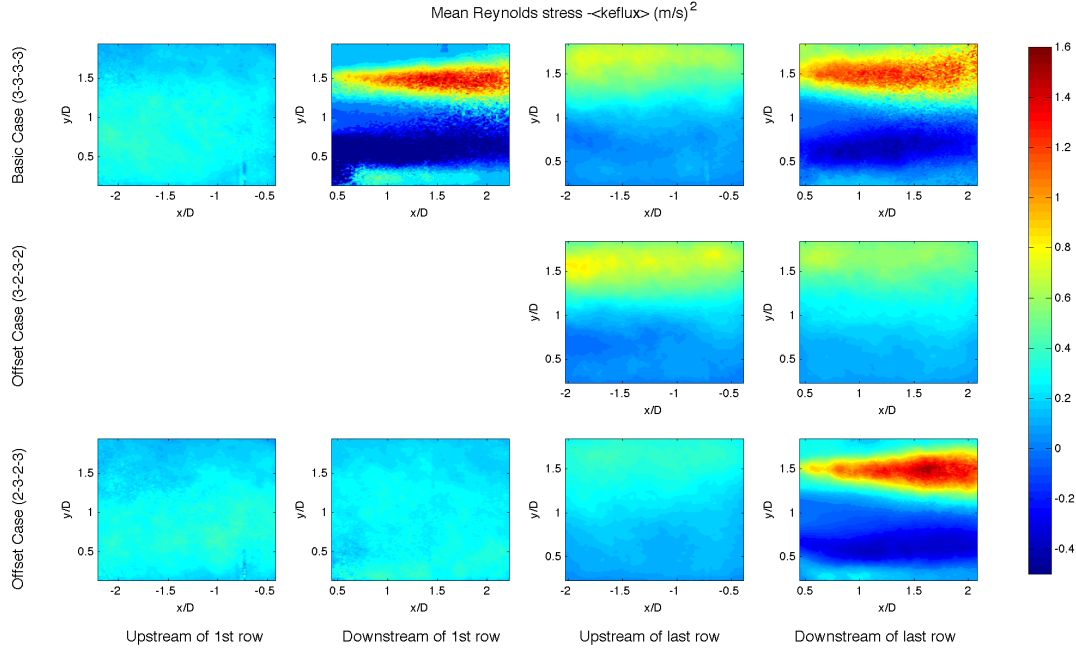


Figure 5.14: Reconstructions of the flux of kinetic energy  $F_{ij}$  for all measurement positions. Plotted data comprised of  $-\bar{uv}$  with only the modes containing the first 50% energy and the mean velocity field  $U$  from SPIV results in Chapter 3.

However, this relationship only demonstrates that the upstream and downstream modes fall off at different rates. For instance, the trendline showing  $\kappa$  for the exit row of the offset case (OC2) shows that the ratio of upstream to downstream POD eigenvalues is lower than the base case for low POD numbers. Thus the energy contained in large structures is more similar on both sides of the wind turbine in the offset case.

The trends shown in figure 5.16 indicate that the ratio of upstream to downstream POD modes varies significantly from case to case. With the power curves in figure 3.2 it can be seen that the exit row of turbines are outperformed by the entrance row turbines in every case, implying that the power extracted from the flow can be connected to the values of  $\lambda$ . This agrees well with theory as the mean flow is significantly reduced by the entrance row of turbines. The trends of  $\lambda$  shown in figures 5.5 and 5.6 above also show that the downstream values of  $\lambda$  are higher at high mode number than upstream. Thus the presence of wind turbines can be seen through increased magnitudes of the eigenvalues corresponding to high mode numbers. In figure 5.16 the exit row turbines (BCB and OC2, green and red, respectively) show that  $\kappa$  is also greater for the poorly performing wind turbines than the entrance row.

Comparing the total turbulent energy through the POD is a matter of summing the

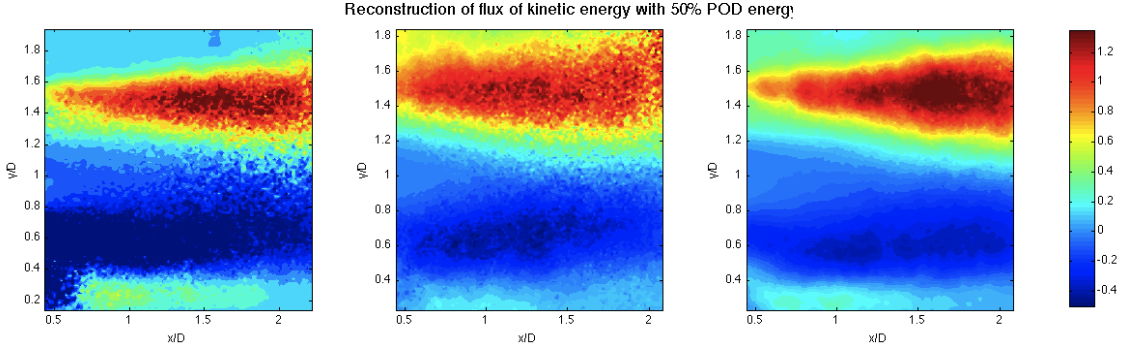


Figure 5.15: Reconstructions of the flux of kinetic energy  $F_{ij}$  for the immediate wake areas. Plotted data is the same as in figure 5.14 From left to right, the entrance and exit rows of the base arrangement, and the exit row of the second offset arrangement (2-3-2-3).

eigenvalues according to equation 1.44. In doing so a global comparison can be made of the turbulence in upstream and downstream positions relative the the turbines. Table 5.3 shows the ratio of eigenvalue summations upstream and downstream of the turbines according to,

$$\mathcal{E} = \frac{E_{upstream}}{E_{downstream}} = \frac{\sum_{n=1}^{2000} \lambda_{upstream}}{\sum_{n=1}^{2000} \lambda_{downstream}} \quad (5.3)$$

Table 5.3: Ratio of sums of eigenvalues in upstream and downstream measurement locations.

Measurement case	$\mathcal{E}$
BCF	0.2100
BCB	0.3439
OC2	0.2933

Comparing the power measurements from Chapter 3 to the values in table 5.3 shows that small magnitudes of  $\mathcal{E}$  correspond to greater power production. This agrees with intuition in that  $\mathcal{E}$  relates the turbulence energy upstream and downstream of the wind turbines. Theory suggests that wind turbines extract energy from the mean flow field, especially the streamwise direction  $U$ . The comparison of turbulence energies adds that the action of clipping turbulent structures into successively smaller ones by the turbine are a means of gauging performance in terms of turbulence alone.

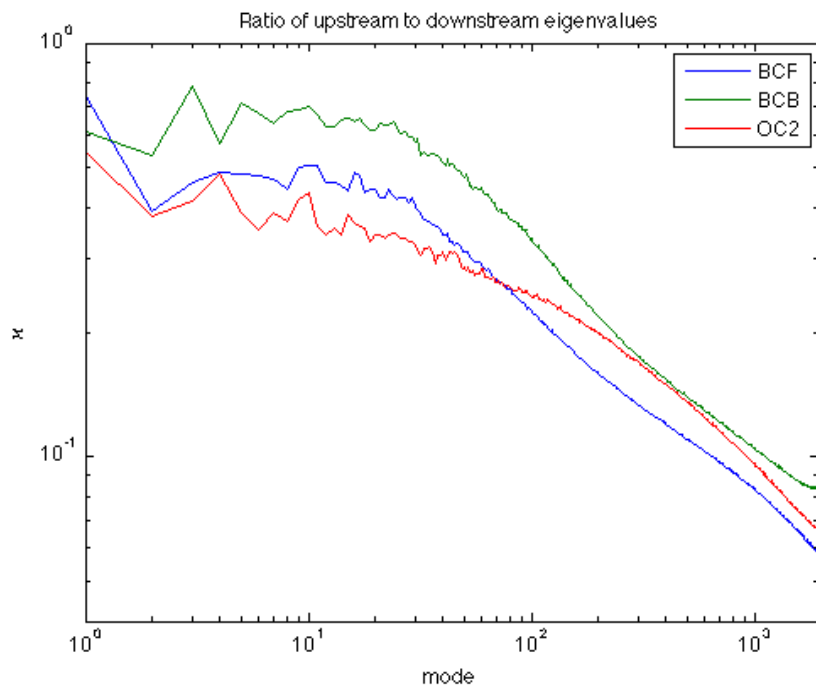


Figure 5.16: Trends comparing each successive value of  $\lambda$  upstream and downstream. The ratio  $\kappa = \lambda_{upstream}/\lambda_{downstream}$  emphasizes the difference of power output of a turbine is linked to small scale organization. A higher ratio of  $\kappa$  at high mode number indicates that *more* energy is converted from the mean flow and large-scale turbulence to small scales.

# Chapter 6

## Conclusion and Discussion of Results

### 6.1 Summary of research

The experiment presented above investigates flow associated with positions immediately upstream and downstream of wind turbines in several array configurations. In the experiment, measurements of the flow were collected with SPIV and velocity statistics show clearly defined wakes and turbulent motion generated by strong gradients and the presence of solid bodies. The wakes show statistically similar behavior in dynamics and structure to many other experiments of the kind.

The kinetic energy flux illustrated by figure 4.15 confirms the net positive entrainment of energy downward from the flow above the turbine canopy. This phenomenon is confirmed by trends in the mean wall-normal velocity,  $V$ , which shows distinct negative regions in the portion of the wakes trailing the top-tip of the rotors. The same phenomenon can be seen in the component of mean vorticity,  $\Omega_3$ , acting in the  $x - y$  plane. In the top of the turbine canopy  $\Omega_3$  demonstrates mean vortical motion is vertically downward from above the canopy and upward from the floor. The net flux of kinetic energy is toward the vertical center of the wake where the momentum deficit is greatest.

It was confirmed in the experiment that wind turbine models produce power depending on the energy contained in the ABL in specific locations. The torque sensing device fixed to the nacelle of the turbines provides direct measurements of mechanical power and reflect power curves similar to those of full scale devices. The power coef-

ficient calculated as a ratio of the mechanical power produced by the turbine and the available power in the mean flow was lower in this experiment than in real cases. It is suspected that further design specification of the turbine rotor can correct this in future measurements. Even at reduced magnitude, the power curves and curves of the power coefficient show distinct differences of production of the turbine models according to the configuration of turbines in the array.

Allowing the turbine wakes to recover more fully toward the ABL by altering the streamwise spacing of devices increases power production of successive turbine models. It was shown by the power measurements in figure 3.2 that there was more than a threefold increase of power production in the exit row turbines of the row-offset configurations. An important benefit of this wind farm design is that the density of turbines is not greatly affected, given a sufficiently large farm. The experiment discussed here was conducted on only a small subset of the total turbines present in a real turbine array.

Applying snapshot POD to the turbulent flow measurements shows concretely that there is a connection between the spacing of the wind turbines within the array and the relative energy content of large turbulent structures. The comparison of eigenvalue distributions in figure 5.5 shows that the rotation of a wind turbine rotor in the ABL leads to large content of energy in intermediate scales of the POD. Similar comparisons of the eigenvalues resulting from the present analysis indicate an apparent concentration of relative energy content in the low POD modes as the wakes within the wind turbine canopy recover. This conforms well to expectations as the flux of kinetic energy pulls high energy fluid into the canopy layer while at the same time, energy is being dissipated from small scales. The net effect of these mechanisms is that energy increases in large scales and decreases in small scales.

The testing of a variety of kernels for the POD indicate clearly the dependence of the accumulation of energy on the inclusion or exclusion of the spanwise component of velocity. The immediate consequence of this is that  $w$  contributes most of its energy to the smaller scales of the turbulent kinetic energy,  $k$ . This is reflected by the statistics computed in Chapter 4, especially those seen in figure 4.12. As discussed in §5.1 and shown in table 5.1, basing the correlation kernel of the POD on instantaneous data rather than fluctuating data leads to leakage of energy from the large scales to small ones in the numerical solution of the eigenvalue problem. This leakage is a numerical

error arising from the difficulty in sorting mean kinetic energy from turbulent kinetic energy within the eigenvalue problem.

Discussed briefly in Chapter 5 is the connection between performance of the wind turbine models and the energy content of  $\lambda$  values resulting from the POD. The power curves shown in figure 3.2 and the values listed in table 5.3 both point to the relationship between power extraction by a wind turbine and the total turbulent kinetic energy ratio,  $\mathcal{E}$ . Because the energy extracted by the turbine is from the mean flow, the ratio of turbulent energy denoted in only an indicator of performance rather than a predictor of power output. The specific relationship between these quantities is the ongoing pursuit of this research.

## 6.2 Future Works

The results suggested in Chapters 3 through 5 are adequate to analyze only the immediate inflow and outflow to the wind turbine positions outlined in the variable arrangement experiment. In the POD of the results a number of deficiencies were discovered in trying to fully characterize the evolution of the turbulent wake. Firstly, the data was limited to a single plane in the spanwise direction. This has lead to a study in which advanced quantities including the flux of kinetic energy could only really be analyzed in the  $x - y$  plane. In this constraint, spanwise derivative relationships were simply out of reach.

Expanding the study to include measurements in the  $y - z$  planes at regularly spaced intervals in the wake of the wind turbine would mitigate open the calculations to include spanwise derivative relationships. Using a similarly sized SPIV window to the one here would also allow simultaneous measurements over the entire rotor area and the wake as it expands downstream. Measurements in this sense would lead to more direct calculations and understanding of the evolution of large structures in the wake. The same measurements would provide a more rigorous means of diagnosing the spanwise velocity fluctuations' contribution to the energy distribution resulting from the POD.

In order to characterize the wakes of wind turbines more fully, simultaneous measurements across a larger span of the area downstream of the turbines are necessary. Correlations between near- and far-wake phenomena are not included in the present research as measurements for far-wake positions (upstream measurements to exit row turbines, for example) are not synchronized with near-wake measurements. To make

such correlations, several PIV windows would have to be aligned in the wake and the resulting vector fields stitched together numerically. The application of snapshot POD to the large fields described here could also provide clues to the recovery of the turbine wakes. As the flow becomes more homogeneous in the wall-normal direction, Fourier modes would become increasingly distinct.

# Bibliography

- [1] R. J. Adrian, K. T. Christensen, and Z.-C. Liu. Analysis and interpretation of instantaneous turbulent velocity fields. *Experiments in Fluids*, 29:275–290, 2000.
- [2] J. F. Ainslie. Calculating the flowfield in the wake of wind turbines. *Journal of Wind Engineering and Industrial Aerodynamics*, 27:213–224, 1988.
- [3] R. Barthelmie, O. Rathmann, S. Frandsen, K. Hansen, E. Politis, J. Prospathopoulos, K. Rados, D. Cabezon, W. Schlez, J. Phillips, A. Neubert, J. G. Schepers, and S. P. van der Pijl. Modelling and measurements of wakes in large wind farms. *Journal of Physics: Conference series*, 75, 2007.
- [4] G. K. Batchelor. *The Theory of Homogeneous Turbulence*. Cambridge University Press, 1953.
- [5] Bal Berkooz, Philip Holmes, and John L. Lumley. The proper orthogonal decomposition in the analysis of turbulent flows. *Annual Reviews of Fluid Mechanics*, 25:539 – 575, 1993.
- [6] J. P. Bonnet, D. R. Cole, J. Delville, M. N. Glauser, and L. S. Ukeiley. Stochastic estimation and proper orthogonal decomposition: Complementary techniques for identifying structure. *Experiments in Fluids*, 17:307 – 314, 1994.
- [7] J. P. Bonnet, J. Delville, M. N. Glauser, R. A. Antonia, D. K. Bisset, D. R. Cole, H. E. Fiedler, J. H. Garem, J. Jeong D. Hilberg, N. K. R. Kevlahan, L. S. Ukeiley, and E. Vincendeau. Collaborative testing of eddy structure identification methods in free turbulent shear flows. *Experiments in Fluids*, 25:197–225, 1998.
- [8] J. Borée. Extended proper orthogonal decomposition: a tool to analyse correlated events in turbulent flows. *Experiments in Fluids*, 35:188 – 192, 2003.
- [9] B. G. Brzek, Raul Bayoan Cal, G. Johansson, and Luciano Castillo. Transitionally rough zero pressure gradient turbulent boundary layers. *Experiments in Fluids*, 44:115–124, 2008.
- [10] Tony Burton, David Sharpe, Nick Jenkins, and Ervin Bossanvi. *Wind Energy Handbook*. John Wiley & Sons, 2001.
- [11] Raul Bayoan Cal, Jose Lebron, Luciano Castillo, Hyung Suk Kang, and Charles Meneveau. Experimental study of the horizontally averaged flow structure in a model wind-turbine array boundary layer. *Journal of Renewable and Sustainable Energy*, 2(013106):1–25, 2010.
- [12] L. P. Chamorro and F. Porte-Agel. A wind-tunnel investigation of wind-turbine wakes: Boundary-layer turbulence effects. *Boundary Layer Metrology*, 132:129–149, 2009.

- [13] J. H. Citriniti and W. K. George. Reconstruction of the global velocity field in the axisymmetric mixing layer utilizing the proper orthogonal decomposition. *Journal of Fluid Mechanics*, 418:137–166, 2000.
- [14] N. J. Cook. Wind-tunnel simulation of the adiabatic atmospheric boundary layer by roughness, barrier and mixing-device methods. *Journal of Industrial Aerodynamics*, 3:157–176, 1978.
- [15] Laurent Cordier and Michel Bergmann. Post-processing of experimental and numerical data. Lecture Series: von Karman Institute for Fluid Mechanics, 2003-04.
- [16] J. Counihan. An improved method of simulating an atmospheric boundary layer in a wind tunnel. *Atmospheric Environment*, 3:197–214, 1969.
- [17] A. Crespo, J. Hernandez, and S. Frandsen. Survey of modelling methods for wind turbine wakes and wind farms. *Wind Energy*, 2:1–24, 1999.
- [18] P. R. Ebert and D. H. Wood. The near wake of a model horizontal-axis wind turbine – i. experimental arrangements and initial results. *Renewable Energy*, 12(3):225–243, 1997.
- [19] S. Frandsen, R. Bathelme, S. Pryor, Ole Tahmann, S. Larsen, and J. Hojstrup. Analytical modelling of wind speed deficit in large offshore wind farms. *Wind Energy*, 9:39–53, 2006.
- [20] Nan Gao and Dan Ewing. Investigation of large scale flow structures in an offset attaching jet using spectral linear stochastic estimation. Technical report, Dalian University of Technology.
- [21] William K. George. Lectures in turbulence for the 21st century.
- [22] J. L. Lumley H. Tennekes. *A First Course in Turbulence*. MIT Press, 1972.
- [23] Nicholas Hamilton, Raul Bayoan Cal, Hyung Suk Kang, and Charles Meneveau. Statistical analysis of kinetic energy entrainment in a model wind turbine array boundary layer. *Jouurnal of Renewable and Sustainable Energy*, 2012 (pending publication).
- [24] J. C. R. Hunt and H. Fernholz. Wind-tunnel simulation of the atmospheric boundary layer: a report on euromech 50. *Journal of Fluid Mechanics*, 70(3):543–559, 1975.
- [25] Peter B. V. Johansson and William K. George. The far downstream evolution of the high-reynolds-number axisymmetric wake behind a disk. part 2. slice proper orthogonal decomposition. *Journal of Fluid Mechanics*, 555:387 – 408, 2006.
- [26] Hyung Suk Kang and Charles Meneveau. Direct mechanical torque sensor for model wind turbines. 2010.
- [27] N.K.-R. Kevlahan, J.C.R. Hunt, and J.C. Vassilicos. A comparison of different analytical techniques for identifying structures in turbulence. *Applied Scientific Research*, 53:339–355, 1994.
- [28] J. Kostas, J Soria, and M. S. Chong. A comparison between snapshot pod analysis of piv velocity and vorticity data. *Experiments in Fluids*, 38:146–160, 2005.
- [29] Z.-C. Liu, R. J. Adrian, and T. J. Hanratty. Reynolds number similarity of orthogonal decomposition of the outer layer of turbulent wall flow. *Physics of Fluids*, 6(8):2815–2819, 1994.
- [30] John L. Lumley. The structure of inhomogeneous turbulent flows. *Atmospheric Turbulence and Wave Propagation*, pages 166–178, 1967.

- [31] Wolfgang Merzkirch. *Flow Visualization, second edition*. Academic Press, Inc, 1987.
- [32] J. Meyers and C. Meneveau. Optimal turbine spacing in fully developed wind-farm boundary layers. *Wind Energy*, 15:305–317, 2012.
- [33] A. S. Monin and A. M. Yaglom. *Statistical Fluid Mechanics, Volume II*. MIT Press, 1975.
- [34] B. Patte-Rouland, G. Lalizel, J. Moreau, and E. Rouland. Flow analysis of an annular jet by particle image velocimetry and proper orthogonal decomposition. *Measurement Science and Technology*, 12:1404–1412, 2001.
- [35] Jakob M. Pedersen. *Analysis of Planar Measurements of Turbulent Flows*. PhD thesis, Technical University of Denmark (DTU), Department of Mechanical Engineering, Building 403, Technical University of Denmark, DK-2800 Lyngby, Denmark, February 2003.
- [36] M. Ragheb. Optimal rotor tip speed ratio. 2011.
- [37] O. Rathmann, S. Frandsen, and R. Barthelmie. Wake modeling for intermediate and large wind farms. 2007.
- [38] Korn Saranyasontorn and Lance Manuel. Low-dimensional representations of inflow turbulence and wind turbine response using proper orthogonal decomposition. *ASME*, pages 1–10, 2005.
- [39] L. Sirovich. Turbulence and the dynamics of coherent structures. part i: Coherent structures. *Quarterly Applied Mathematics*, 45(3):561–571, 1987.
- [40] H. Snel. Review of aerodynamics for wind turbines. *Wind Energy*, 6:203–211, 2003.
- [41] Murat Tutkun, Peter B. V. Johansson, and William K. George. Three-component vectorial proper orthogonal decomposition of axisymmetric wake behind a disk. *AIAA*, 46(5):1118 – 1134, May 2008.
- [42] L. J. Vermeer, J. N. Sorensen, and A. Crespo. Wind turbine wake aerodynamics. *Progress in Aerospace Sciences*, 39:457–510, 2003.
- [43] J. Whale, K.H. Papadopoulos, C. G. Anderson, C. G Helmis, and D. J. Skyner. A study of the near wake structure of a wind turbine comparing measurements from laboratory and full-scale experiments. *Solar Energy*, 56(6):621–633, 1996.
- [44] W. Yue, Charles Meneveau, M. B. Parlange, W. Zhu, Hyung Suk Kang, and J. Katz. Turbulent kinetic energy budgets in a model canopy: comparisons between les and wind-tunnel experiments. *Environmental Fluid Mechanics*, 2008.